

1-1-2003

## A computational study on mixing of two-phase flow in microchannels

Farshid Bondar  
Iowa State University

Follow this and additional works at: <https://lib.dr.iastate.edu/rtd>

### Recommended Citation

Bondar, Farshid, "A computational study on mixing of two-phase flow in microchannels" (2003).  
*Retrospective Theses and Dissertations*. 19907.  
<https://lib.dr.iastate.edu/rtd/19907>

This Thesis is brought to you for free and open access by the Iowa State University Capstones, Theses and Dissertations at Iowa State University Digital Repository. It has been accepted for inclusion in Retrospective Theses and Dissertations by an authorized administrator of Iowa State University Digital Repository. For more information, please contact [digirep@iastate.edu](mailto:digirep@iastate.edu).

**A computational study on mixing of two-phase flow in  
microchannels**

by

Farshid Bondar

A thesis submitted to the graduate faculty  
in partial fulfillment of the requirements for the degree of  
MASTER OF SCIENCE

Major: Mechanical Engineering

Program of Study Committee:  
Francine Battaglia, Major Professor  
Rodney O. Fox  
Michael G. Olsen

Iowa State University

Ames, Iowa

2003

Copyright © Farshid Bondar, 2003. All rights reserved.

Graduate College  
Iowa State University

This is to certify that the Master's thesis of  
Farshid Bondar  
has met the thesis requirements of Iowa State University

Signatures have been redacted for privacy

---

To my mother, Farideh, and my sister, Farnoush,  
for their understanding of a *chaotic* person.

## TABLE OF CONTENTS

<b>LIST OF TABLES</b> . . . . .	vii
<b>LIST OF FIGURES</b> . . . . .	viii
<b>NOMENCLATURE</b> . . . . .	xii
<b>ACKNOWLEDGEMENTS</b> . . . . .	xvi
<b>ABSTRACT</b> . . . . .	xviii
<b>CHAPTER 1 INTRODUCTION</b> . . . . .	1
1.1 Background and Motivation . . . . .	2
1.2 Objective and Outline of Thesis . . . . .	3
<b>CHAPTER 2 LITERATURE REVIEW</b> . . . . .	5
2.1 Microfluidics . . . . .	5
2.1.1 Gas flows in microfluidics . . . . .	6
2.1.2 Liquid flows in microfluidics . . . . .	8
2.2 Micromixers . . . . .	12
2.3 Chaotic Mixing . . . . .	14
2.4 Chaotic Micromixers . . . . .	18
<b>CHAPTER 3 PHYSICAL MODEL, GOVERNING EQUATIONS, AND NUMERICAL FORMULATION</b> . . . . .	21
3.1 The Mixture Model . . . . .	21
3.2 Governing Equations . . . . .	23

3.3	Numerical Formulation . . . . .	24
3.3.1	Segregated solver . . . . .	25
3.3.2	Second-order upwind scheme . . . . .	27
3.3.3	Central-difference scheme . . . . .	27
3.3.4	Under-relaxation factors . . . . .	28
3.3.5	SIMPLE method . . . . .	29
3.3.6	Residuals in segregated solver . . . . .	30
<b>CHAPTER 4 STATEMENT OF PROBLEM AND COMPUTATIONAL</b>		
<b>CONSIDERATIONS . . . . .</b>		<b>32</b>
4.1	Statement of Problem . . . . .	32
4.1.1	Geometry of microchannels . . . . .	32
4.1.2	Physical properties of selected liquids . . . . .	36
4.1.3	Initial and boundary conditions . . . . .	37
4.2	Computational Considerations . . . . .	38
4.2.1	Grid resolution tests . . . . .	38
4.2.2	Steady-state calculations . . . . .	41
4.2.3	Computational performance . . . . .	41
<b>CHAPTER 5 RESULTS . . . . .</b>		<b>43</b>
5.1	Mixing Index . . . . .	43
5.2	Pressure Distribution . . . . .	60
5.3	Evolution of Path Lines and Onset of Chaos . . . . .	61
5.4	Correlation Between Quantitative and Qualitative Discussion of Mixing . . . . .	68
<b>CHAPTER 6 CONCLUDING REMARKS AND RECOMMENDA-</b>		
<b>TIONS . . . . .</b>		<b>71</b>
6.1	Conclusions . . . . .	71
6.2	Open Questions . . . . .	72

BIBLIOGRAPHY . . . . .	74
BIOGRAPHICAL SKETCH . . . . .	87

**LIST OF TABLES**

Table 4.1	Mesh sizes used for grid resolution tests. . . . .	38
Table 5.1	Total pressure drop (Pascal) in various microchannels between sections <i>A</i> and <i>C</i> for the Reynolds numbers ranging between 6 and 96. . . . .	60

## LIST OF FIGURES

Figure 3.1	Control volume used to illustrate discretization of a scalar transport equation. . . . .	25
Figure 4.1	Schematic of microchannels: (a) straight, (b) square-wave, (c) serpentine, and (d) twisted microchannel. The distance between inlet and outlet along the centerline is 5.9 mm in all microchannels.	33
Figure 4.2	Dimensions of each block to build different types of bends in square-wave, serpentine, and twisted microchannels. 300 $\mu\text{m}$ in $x$ - and $y$ -directions and 150 $\mu\text{m}$ in $z$ -direction were considered to be consistent with the study of Liu et al. [9]. . . . .	34
Figure 4.3	Schematic of flow direction in (a) straight, (b) square-wave, (c) serpentine and (d) twisted microchannels. . . . .	35
Figure 4.4	Plug flows of water and alcohol side by side as the inlet boundary conditions. . . . .	37
Figure 4.5	Centerline of the mid cross-section of the serpentine microchannel.	39
Figure 4.6	Grid resolution test for serpentine microchannel at $\text{Re}=70$ using Richardson extrapolation. . . . .	40

Figure 5.1	The location of cross sections $A$ , $B$ , and $C$ , where mixing index is quantified, in each microchannel: (a) straight, (b) square-wave, (c) serpentine, and (d) twisted microchannel. The distance between inlet and cross sections $A$ , $B$ , and $C$ along the centerline are 0.8, 2.95, and 5.1 mm for all microchannels. . . . .	44
Figure 5.2	Mixing index versus centerline distance in the straight microchannel for various Reynolds numbers. . . . .	45
Figure 5.3	Mixing index versus centerline distance in the square-wave microchannel for various Reynolds numbers. . . . .	46
Figure 5.4	Mixing index versus centerline distance in the serpentine microchannel for various Reynolds numbers. . . . .	47
Figure 5.5	Mixing index versus centerline distance in the twisted microchannel for various Reynolds numbers. . . . .	48
Figure 5.6	Mixing index versus centerline distance in different microchannels for the Reynolds number of 6. . . . .	48
Figure 5.7	Mixing index versus centerline distance in different microchannels for the Reynolds number of 12. . . . .	49
Figure 5.8	Mixing index versus centerline distance in different microchannels for the Reynolds number of 35. . . . .	50
Figure 5.9	Mixing index versus centerline distance in different microchannels for the Reynolds number of 70. . . . .	51
Figure 5.10	Mixing index versus centerline distance in different microchannels for the Reynolds number of 96. . . . .	52
Figure 5.11	Contour plots of density at sections $A$ , $B$ , and $C$ in (a) straight, (b) square-wave, (c) serpentine, and (d) twisted microchannels for the Reynolds number of 6. . . . .	53

Figure 5.12	Contour plots of density at sections <i>A</i> , <i>B</i> , and <i>C</i> in (a) straight, (b) square-wave, (c) serpentine, and (d) twisted microchannels for the Reynolds number of 12. . . . .	55
Figure 5.13	Contour plots of density at sections <i>A</i> , <i>B</i> , and <i>C</i> in (a) straight, (b) square-wave, (c) serpentine, and (d) twisted microchannels for the Reynolds number of 35. . . . .	56
Figure 5.14	Contour plots of density at sections <i>A</i> , <i>B</i> , and <i>C</i> in (a) straight, (b) square-wave, (c) serpentine, and (d) twisted microchannels for the Reynolds number of 70. . . . .	58
Figure 5.15	Contour plots of density at sections <i>A</i> , <i>B</i> , and <i>C</i> in (a) straight, (b) square-wave, (c) serpentine, and (d) twisted microchannels for the Reynolds number of 96. . . . .	59
Figure 5.16	Path lines in the straight microchannel at the Reynolds number of 6. Flow is from left to right. . . . .	63
Figure 5.17	Path lines in the square-wave microchannel at the Reynolds number of 6. Flow is from left to right. . . . .	63
Figure 5.18	Path lines in the serpentine microchannel at the Reynolds number of 6. Flow is from left to right. . . . .	64
Figure 5.19	Path lines in the twisted microchannel at the Reynolds number of 6. Flow is from left to right. . . . .	64
Figure 5.20	Path lines in the straight microchannel at the Reynolds number of 35. Flow is from left to right. . . . .	66
Figure 5.21	Path lines in the square-wave microchannel at the Reynolds number of 35. Flow is from left to right. . . . .	66
Figure 5.22	Path lines in the serpentine microchannel at the Reynolds number of 35. Flow is from left to right. . . . .	67

Figure 5.23	Path lines in the twisted microchannel at the Reynolds number of 35. Flow is from left to right. . . . .	67
Figure 5.24	Mixing index versus Reynolds number in each microchannel at section <i>B</i> . . . . .	69
Figure 5.25	Mixing index versus Reynolds number in each microchannel at section <i>C</i> . . . . .	69

## NOMENCLATURE

$A, B$	material volumes
$A, B, C$	cross sections
$\vec{A}$	surface area vector
$\mathcal{C}$	centerline
$D$	diameter
$F$	force
$I$	identity matrix
$J$	mass flux
$Kn$	Knudsen number
$N$	number
$R$	residual
$\mathcal{R}$	region
$Re$	Reynolds number
$S$	source term
$T$	specific time
$\bar{U}$	average velocity
$V$	cell volume
$a$	weighting factor
$c$	cell center
$d_f$	coefficient in the momentum-weighted averaging formulation

$g$	gravitational acceleration
$\iota$	unit vector in normal direction
$n$	order of accuracy
$p$	pressure
$p_2$	secondary phase
$\vec{r}$	vector direction from the cell centroid towards the face centroid
$\vec{s}$	vector direction from the upstream cell centroid towards the face centroid
$t$	time
$u$	streamwise velocity
$v_m$	mass-averaged velocity
$\vec{v}$	velocity vector field
$x$	streamwise direction
$y$	cross-stream direction
$z$	spanwise direction

## Greek Symbols

$\Gamma$	diffusion
$\Phi$	flow
$\alpha$	volume fraction
$\eta$	under-relaxation factor
$\mu$	viscosity
$\rho$	density
$\bar{\bar{\tau}}$	stress tensor
$\phi$	scalar

## Superscripts

*	guessed value
'	corrected value

## Subscripts

<i>CD</i>	central difference
<i>H</i>	hydraulic
<i>P</i>	cell
<i>UP</i>	upwind
<i>f</i>	face
<i>i</i>	cell index
<i>iter</i>	iteration
<i>k</i>	phase
<i>m</i>	mixture
<i>n</i>	normal
<i>nb</i>	neighboring cells
<i>old</i>	old value
<i>sect</i>	section

## Other Symbols

$\Delta$	displacement
----------	--------------

$\nabla$	gradient operator
$\nabla \cdot$	divergence operator

## Abbreviations

CFD	computational fluid dynamics
MEMS	micro-electro-mechanical systems
SIMPLE	semi-implicit method for pressure-linked equations

## ACKNOWLEDGEMENTS

There is very little work that anyone could do solely. So it is with this Master's thesis. I could not have written it without the help and encouragement of others. In citing them, I shall start with my *indefatigable* supervisor, Dr. Francine Battaglia. Not only did she understand me throughout for two years when I was frustrated by my *chaotic* ideas, but also she was always present to help me explore things in perspective. In addition, she generously provided me the financial support since the beginning of my graduate studies. I am indebted to her for always.

I would like to sincerely thank my mother, Farideh, and my sister, Farnoush, for their love, patience, and understanding of *higher education* during the course of my life. Without their encouragement and support, I would not be able to achieve any of my goals.

I wish to express my gratitude to Dr. Rodney O. Fox and Dr. Michael G. Olsen, not only for serving as my committee members, but for the knowledge which I gained through the *excellent* courses they taught. Also, I would like to thank Dr. Fox for adding me to the Fluent software users of his group.

I would like to gratefully acknowledge Dr. James J. Coyle at High Performance Computing Center at Iowa State University and Sarah Monahan at Chemical Engineering Department for their invaluable helps with CFDLib code although I have not included any simulation results by this code in the present work. The provision of computer resources by the High Performance Computing Center at Iowa State University is acknowledged.

This thesis would not have been conceived without the stimulus of two individuals: my senior thesis supervisor at the Sharif University of Technology, Dr. Mohammad Taeibi-Rahni, who never obstructed my *vision*, and my friend and mentor for several years, Dr. Shahin Keynoush, who acquainted me with the consequences of a *butterfly*, even though astonishment of his disappearance still exists.

A warm thank you goes to my friends and colleagues at CFD lab in mechanical engineering department: Anup, John, Jin, Nan, Andrew, Ross, Xiaohang, Kunlun, Joon, Chunjian, Yang, Xiaofeng, Zhaohui, Steve, Ravikanth, Madhusudan, Ying, Hong Wai, and Arun. They not only helped me to find my way and pass through difficult times which I had in Ames, but also encouraged me to pursue my ideas. I had a *memorable* time with them.

## ABSTRACT

The passive mixing of water and alcohol, as two fluids with different densities, is carried out computationally in three-dimensional microchannels. Four designs of microchannels are considered to investigate the efficiency of mixing for Reynolds numbers ranging between 6 and 96. In a straight-type of microchannel, mixing is very poor. In a square-wave-type of microchannel, mixing is marginally better than the straight microchannel. Mixing in serpentine-type and twisted-type of microchannels develops considerably better than the first two microchannels, especially at higher Reynolds numbers. However, in the twisted microchannel, mixing index is substantially larger compared to the serpentine microchannel for the Reynolds number of 35. The higher mixing index implies the occurrence of spatially chaotic flows with a higher degree of chaos comparing with the case of serpentine microchannel. The results are compared quantitatively and qualitatively in Lagrangian and Eulerian frameworks and a correlation between Lagrangian chaos and Eulerian chaos is concluded.

## CHAPTER 1 INTRODUCTION

Richard Feynman, the 1965 Nobel prize winner in Physics, in his prophetic lecture “There’s plenty of room at the bottom” at the annual meeting of the American Physical Society on December 29th 1959 [1], addressed novel applications in microscale science and engineering. In a followup lecture in 1983 at the Jet Propulsion Laboratory, Feynman revisited this subject, anticipating the development and use of some of today’s Micro-electro-mechanical systems (MEMS) [2].

MEMS refer to devices which have a characteristic length of less than 1 mm but more than 1  $\mu\text{m}$ . Generally, these systems combine electrical and mechanical components and are fabricated using integrated circuit batch-processing technologies [3]. Over the past decade, numerous MEMS have been designed and widely used in different fields, such as biomedical, chemical, optical, and aeronautical technologies.

Another scientific subject which shed light on science and technology was the theory of chaos initiated two years before Feynman’s prediction of MEMS. In 1963, Edward Lorenz revealed a phenomenon in fluid dynamics now broadly known as chaos theory [4]. He showed that due to nonlinearities and sensitivity of the fluid dynamics governing equations, which are deterministic equations, the solution of the Navier-Stokes equations can be chaotic, and seemingly unpredictable under very specific initial conditions. Since Lorenz’s discovery, many researchers focused on chaotic dynamics of fluids and showed that chaotic behavior can be a common occurrence in fluidic systems under specific initial and boundary conditions.

## 1.1 Background and Motivation

Microfluidics is one of the categories of the multidisciplinary field of MEMS. The advantages of microfluidics such as manipulation with fast response times, flow control of small fluid volumes, and selectively have been addressed. However, the insight into microfluidics is still lacking as particular circumstances exist when dealing with these systems.

Principally, the Navier-Stokes equations are applied to describe fluid flows at the macroscale. However, in microfluidics, since the dimension of flow is on the order of tens of microns, some physical conditions, which are typically dismissed in conventional macroflows, need to be considered. One of these conditions is the dominant surface effects on flows at the microscale. Generally, surface effects in microdevices induce very high viscous forces. These viscous forces are so substantial that the occurrence of microscale mixing has been a challenging topic for researchers since the beginning of microfluidics.

Basically, the nature of mixing can be divided into two categories depending on whether the Reynolds number of the flow is small or large. The Reynolds number is defined as the ratio of inertial forces to viscous forces in the flow. At high Reynolds numbers, generally on the order of 1000 and more, internal flow is often turbulent. A turbulent flow readily contributes toward mixing by intense velocity fluctuations existing in both time and space over a large range of scales, resulting in highly enhanced transport properties [5]. However, at low Reynolds numbers, typically on the order of 100 or less, in which viscous forces do play an important role and dominate inertial forces, those effects which exist in turbulent flow are absent.

Nevertheless, micromixers are widely needed for effective mixing of fluids on the microscale although the classical methods used in macroscale to achieve mixing are not available at the microscale. Low Reynolds number laminar flows in microfluidics pre-

clude turbulence as previously discussed. The operation of active micromixers which involve moving parts is too troublesome, if not unfeasible, in microscale flows. Even at microscales, mixing based on intermolecular diffusion occurs at a very slow rate. These particular characteristics impact the efficient design and operation of micromixers significantly. Therefore, finding an appropriate approach on which the design of micromixers can be built is a challenging and creative task for engineers.

Chaotic advection, first introduced by Aref [6], has opened a new framework for the efficient mixing of fluids at very low Reynolds numbers in the absence of turbulence [7]. It has been proved that if chaotic advection occurs, stretching and distortion of fluid elements in the laminar regime can result in enhanced transport and therefore good mixing. Indeed, it appears that in many laminar flows, chaotic advection may be the rule rather than the exception [8]. However, amongst the concepts that are helpful in the context of laminar mixing, chaotic mixing has been a promising phenomenon so far.

Is there any possibility to apply chaotic advection to mix fluids in microscale flows? If so, is it possible to design a passive micromixer which has no moving part and possesses good mixing? What are those conditions for which transition to chaos occurs at the microscale? These are questions which rise in conjunction when analyzing micromixers and chaotic mixing.

## 1.2 Objective and Outline of Thesis

The objective of the present work is to utilize computational fluid dynamics (CFD) to investigate mixing in a variety of microchannel designs. These microchannels have been previously studied experimentally by Liu et al. [9] and Stremler et al. [10]. In fact, CFD provides an alternative means as opposed to experimental research to study fluid flows. Maybe the most important advantage of CFD to experimental fluid mechanics is that CFD can provide data which are costly and difficult to obtain experimentally due

to limitations with experimental techniques. For example, when the scale goes down (such as MEMS and nanotechnology), CFD is a faster and less costly solution.

To furnish the proposed investigation, the mixing of water and liquid alcohol, as two liquids with different densities, are considered. The variations of density along the microchannels are measured to diagnose the mixing index. Furthermore, pressure drop along the microchannels is studied since configurations of microchannels have different types of bends. Also, the possibility and role of chaotic mixing in microchannels are considered. The ultimate goal is to address the relationship between Eulerian chaos and Lagrangian chaos in three-dimensional dynamical systems.

Chapter 2 is a detailed literature survey on microfluidics, micromixers, chaotic mixing, and chaotic micromixers. Physical models, governing equations, and numerical formulations are discussed in Chapter 3. In Chapter 4 statement of problem is explained in terms microchannel geometry, properties of selected fluids, and initial and boundary conditions. For the sake of completeness, included in Chapter 4 are also the results of grid resolution tests and computational performance. Results are presented quantitatively and qualitatively in Chapter 5 in detail. Chapter 6 consists of concluding remarks and recommendations for future work.

## CHAPTER 2 LITERATURE REVIEW

The purpose of this chapter is to review briefly the background and recent advances in microfluidics, micromixers, and chaotic mixing. Because each of these subjects has its own specifications, they are presented separately in the following sections. In the last section of this chapter, the relatively new subject of chaotic micromixing is reviewed.

### 2.1 Microfluidics

Microchannels, micropumps, microturbines, microheat exchangers, microbearings, and microvalves are some examples of microdevices involving the flows of liquids and/or gases. The rapid progress in fabrication and utilization of MEMS during the last decade does not correspond to our delayed understanding of the unconventional physics in the operation of these microscale devices. As an example, fluid flow in microdevices differ from those in macroscales mainly because surface effects dominate in minute devices. To find the significance of surface effects, one can consider the surface-to-volume ratio in micro and macroscales. As an example, the ratio for a machine with a characteristic length of 1 m is  $1 \text{ m}^{-1}$ , while the ratio for a MEMS device with a characteristic length of  $1 \mu\text{m}$  is  $10^6 \text{ m}^{-1}$ . In addition, viscous dissipation is very significant in microfluidics, and under normal circumstances the Reynolds number is on the order of 1 or 10. The million-fold increase in surface area relative to the mass of the minute devices and low Reynolds numbers substantially affect the transport of mass, momentum and energy through these systems.

The small length-scale of microdevices may invalidate the continuum approximation altogether [11,12]. Slip flow, thermal creep, rarefaction, viscous dissipation, compressibility, intermolecular forces and other unconventional effects may have to be taken into account, preferably using only first principles such as conservation of mass, Newton's second law, and conservation of energy. Therefore, in dealing with fluid flow through microdevices, one is faced with the question of how to proceed to obtain solutions to the problem accurately.

The two basic categories of fluids are either liquids or gases. At a fluid-solid interface, the operation of MEMS for liquids and gases cannot always be predicted from conventional flow models such as the Navier–Stokes equations with, for instance, no-slip boundary conditions, as routinely and successfully applied for larger flow devices. For MEMS applications, the possibility of non-equilibrium flow conditions and the consequent invalidity of the Navier–Stokes equations and the no-slip boundary conditions are anticipated [12].

### 2.1.1 Gas flows in microfluidics

For gases, microfluid mechanics has been studied by incorporating slip boundary conditions, thermal creep, viscous dissipation as well as compressibility effects into the continuum equations of motion. Knudsen studied gas flow through glass capillary tubes in the transition and free molecular regimes in 1909 and 1910 [13–15] which led to the well-known Knudsen number. This number is defined as the ratio between the mean free path and the characteristic length of a channel. The different Knudsen number regimes of gaseous flows can be summarized as [12]:

- 1) Euler equations (neglect molecular diffusion):  $Kn \rightarrow 0$
- 2) Navier–Stokes equations with no-slip boundary conditions:  $Kn \leq 10^{-3}$
- 3) Navier–Stokes equations with slip boundary conditions:  $10^{-3} \leq Kn \leq 10^{-1}$

- 4) Transition regimes:  $10^{-1} \leq Kn \leq 10$   
 5) Free-molecule flow:  $10 < Kn$

For rarefied gas flows ( $Kn \geq 10^{-3}$ ) in microchannels the material and surface roughness, predominantly govern the fluid-wall interactions. The interactions of gas molecules with walls, which introduce the definitions of thermal and momentum accommodation coefficients, have been studied with molecular-based simulations by Mo and Rosenberger [16], Allen and Tildesley [17], Koplik et al. [18,19], and Lee et al. [20]. Results of these studies have substantiated the application of slip conditions for gaseous flows in microscales.

In an analytical-numerical study by Jie et al. [21] a solution for the two-dimensional steady compressible gas flow in MEMS was proposed. A second-order slip boundary condition of velocity on the walls was taken into account which eliminated the need for an empirical parameter in a formulation proposed by Beskok [22]. This model was employed in the simulation of three fundamental types of flows: Couette flow, rectangular channel flow, and axisymmetric pipe flow, the later two being pressure-driven. A general agreement with experimental results of Pong et al. [23] and computational results of Beskok [24] was shown for pressure-driven channel flow. However, there are differences in terms of magnitude for the estimated values. For Couette flow and axisymmetric pipe flow, no comparisons with experimental or numerical investigations were performed.

On the other hand, Karniadakis and Beskok [25,26] studied rarefied gas flows in microfluidic devices with smooth surfaces. They introduced a general physics-based model for the slip boundary condition in the entire Knudsen number based on diffuse reflection. The model was compared with both atomistic models and experimental data which were in good agreement. Also, Karniadakis et al. [26,27] have developed a high-order spectral element method to simulate gas flow in microfluidic devices and the result of their endeavor is the  $\mu$ Flow code.

One may argue that at such low Reynolds numbers the convective effects should be neglected, but in complex geometries with abrupt turns the effects may be substantial and thus they need to be taken into account [28]. For this reason, the effects of bends in microfluidics have been investigated by a number of researchers.

It was measured experimentally by Lee et al. [20] that secondary gaseous flows can form in microchannels with different types of junctions, bends, and curves. However, these secondary flows, which cause separations, are not expected because of very low Reynolds number. A model for mass flow rate proposed by Arkilic et al. [29] was corrected by Lee et al. [20] to account for the development of secondary flows and slip flow effects. However, flow visualizations were not presented to show the formation of secondary flows.

Stone and Kim [30] have highlighted the important influence of bends in microchannels since bends occur frequently when maximizing the use of space in a design of a microdevice. In addition, they have emphasized the need to define accurately single-phase microflows from two- or multiphase microflows. Also as the length scale of geometry is reduced, additional length scales associated with the surface forces become more significant in the overall response. For instance, since the pressure drop as a function of flow rate varies as the inverse fourth power of the radius, a very small change in the dimension transverse to the flow, such as manufacturing imperfections or particulates adhering to the wall surface, produces large changes in the flow. Because of these reasons, the concept of geometric features and ratios in relation to Reynolds number require further analysis.

### **2.1.2 Liquid flows in microfluidics**

In the case liquid flows, there is not a non-dimensional number, like the Knudsen number for gas flows. In fact, microfluid mechanics of liquids is more complicated. Liquids do not have a well advanced molecular-based theory as that for gases. The concept

of mean free path is not applicable for liquids and the conditions under which a liquid flow fails to be in quasi-equilibrium state are not well defined. The molecules are much more closely packed at normal pressures and temperatures, and the attractive or cohesive potential between liquid and solid plays a dominant role when the characteristic length of the flow is sufficiently small. It has not been well understood, from first principles, the conditions under which the no-slip boundary condition becomes inaccurate. Experiments indicate that the simple relations that are taken for granted fail to accurately model liquid flows. In cases when the traditional continuum model fails to provide accurate predictions, expensive molecular dynamics simulations seem to be the only first-principle approach available to relatively characterize liquid flows in microdevices. Such simulations are not yet feasible for realistic flow extent. As a consequence, the microfluid mechanics of liquids is much less developed than that for gases.

The first paper describing liquid flow in microtubes with diameters ranging from  $30\ \mu\text{m}$  to  $150\ \mu\text{m}$  was published by Poiseuille [31] in 1846. The studies of Poiseuille led to the well-known relationship between flow rate, pressure drop, and tube geometry although he seemed to be unaware of the viscosity effect at microscales at that time.

Koplik et al. [18] established the no-slip boundary condition of simple liquids from experimental studies and molecular dynamics simulations. In an investigation by Santiago et al. [32], steady velocity fields of deionized water flows in microfluidic devices were studied experimentally by. The no-slip boundary condition has been reported near walls in a simple Hele–Shaw flow field for a characteristic velocity and Reynolds number of  $50\ \mu\text{m}/\text{s}$  and  $0.0003$ , respectively. To analyze and simulate interdiffusion and resulting chemical interaction of human sera in T-microfluidic-sensors, Kamholz et al. [33] considered no-slip boundary conditions for microchannels with width and depths on the orders of  $100\ \mu\text{m}$  and  $10\ \mu\text{m}$ . Whitesides and Strook [34] reported that the effect of slip is negligible when liquids flow through microchannels. Steady Stokes water flow through a  $30\ \mu\text{m} \times 300\ \mu\text{m}$  glass microchannel was investigated experimentally by Meinhart et

al. [35]. The no-slip boundary was observed for a characteristic velocity of 1.5 mm/s. In another study, Tretheway and Meinhart [36] showed that the no-slip boundary condition is a valid assumption for a hydrophilic liquid flowing over a clean hydrophilic surface. However, in the hydrophobic coated microchannel they observed slip on the walls. Thus, modeling fluid flow at the microscale with the assumption of no-slip may or may not be accurate, and will depend on the interactions between the fluid and the surface properties of the wall.

Even though the no-slip boundary condition for liquid microflows have been examined by many researchers, it does not make the study of liquid flow through microchannels a routine process since surface effects dominate the fluid flowing through these miniature devices. The problem seems to be even more complex than gas flows in microdevices.

The transitional Reynolds number of liquid flows through microchannels diminishes as the size of microchannels decreases [37–39]. Peng et al. [38] illustrated the key roles of hydraulic diameter and aspect ratio of rectangular microchannels with Reynolds numbers in the range of 200–700 to analyze different regimes of water streams. As the hydraulic diameter decreases, the critical Reynolds number for the transition from laminar to turbulent flows increases. More importantly, the channel height to width of 0.5 has been suggested with confidence as an optimum parameter in which the flow friction has a minimum value. This investigation includes two empirical expressions of friction factors for laminar and turbulent flows of water in microscales which are different from classical friction factors. Xu et al. [39] studied computationally water flow in microtubes with diameters between 50 and 130  $\mu\text{m}$ . Reynolds numbers considered in the range of 1000 and 2000 were assumed to be in the turbulent region based on an experimental study of Mala and Li [40]. A one-equation turbulent model was introduced by considering no-slip boundary condition on the walls. Numerical results for pressure gradient along the channel were compared with experimental results of Mala and Li [40] which were in good agreement. However, Mala and Li had mentioned the possibility of surface

roughness effects of the microtubes on turbulent behavior which was not accounted by Xu et al. [39].

Another issue involved with liquids flowing through microdevices is the apparent viscosity of liquids. The assumption that viscosity of liquids, such as water, silicon oil and alcohol, in microfluidics is independent of the dimension of microchannel may not be valid [41]. It is interesting to note that the viscosity seems to be lower, not higher, in the narrower microchannels [11].

In the realm of multiphase flows, Triplett et al. [42, 43] examined experimentally two-phase flows in microchannels with hydraulic diameters in the range of 1–1.5 mm. Using air and water for velocities in the ranges of 0.02–80 m/s and 0.02–8 m/s, respectively, physical features of flow, void fraction, and two-phase frictional drop were studied. The results were compared with experimental investigations and models available in macroscales. Poor agreement was found although the reasons were not discussed extensively. The need for intensive investigations in the realm of two-phase flows in microscales were concluded due to unknown behavior of these types of flows.

Molecular dynamics method is another tool to study liquid microflows although the method is limited to extremely small flow extents. This method is being used to model liquid flows in dimensions of the order of 100 nm or less and for time intervals of a few nanoseconds [17, 19, 26]. This model is suitable to simulate flows with high shear rates and in the region in which continuum or the Newtonian hypothesis may not be valid. Karniadakis and Beskok [26] based on the molecular-based simulations of liquid flow of Thompson and Troian [44] suggested that the behavior of liquids is non-Newtonian in the vicinity of walls at high shear rates (even for Newtonian fluids). Gad-el-Hak [12] mentioned that this behavior may be applicable in MEMS and more research is needed. Another approach to microflows is Lattice Boltzmann method which is appropriate both for gas and liquid microflows as well as for multiphase microflows [45].

Rectangular channels with cross-sectional dimensions on the order of hundreds of

microns involving the flow of liquids, like water, are well suited to the standard continuum description of transport processes and incompressible Navier–Stokes equations, even though surface forces play a more important role [30, 46, 47]. In addition, typical microchannel length scales are much larger than the molecular spacing of simple liquids. Hence, the no-slip boundary condition should be valid. Even if slip effects exist, the slip length is so small that the no-slip condition holds. In nanotechnology, however, that may not be the case.

## 2.2 Micromixers

To study mixing phenomenon, it is better to define mixing mathematically and physically first. Consider a flow region  $\mathcal{R}$  and two other regions inside  $\mathcal{R}$ : a material volume  $\mathcal{A}$  and another volume, fixed in space,  $\mathcal{B}$ . The system mixes if there is a time  $T$ , so that for any time  $t > T$ ,  $\Phi_t(\mathcal{A}) \cap \mathcal{B} \neq \emptyset$  [48], where  $\Phi_t$  denotes flow. However, this definition does not describe the physical meaning of mixing. Principally, basic physical processes occurring during mixing are divided into three categories: (a) stretching and folding; (b) diffusion; and (c) break up.

From the beginning of MEMS, mixing phenomenon, as one of the most fundamental, challenging, and mysterious mechanisms in fluid mechanics, has been investigated by researchers. Schwesinger et al. [49] examined experimentally the effects of the consequent vertical/horizontal fork-shaped microchannels on mixing. Basically, they applied the concept of breakup [48] for the mixing enhancement. A liquid stream through each unit of their device, which was on the order of  $500 \mu\text{m}$ , was divided perpendicular to the boundary layer, united in a stable formation and separated again perpendicular to the boundary layers. They found that obstacles constructed in the channel do not lead to turbulence in the flow. Also they showed that a twisting of the fluid layers can not occur due to the highly laminar flow. On the other hand, by increasing contact

area and decreasing diffusion length of two liquid streams, fast mixing in a micromixer was investigated computationally and experimentally by Branebjerg et al. [50]. The characteristic length of their micromixer was of the order of  $10\ \mu\text{m}$ . In order to avoid cross-flows before lamination, they used a separation plate in their mixer. Reynolds numbers less than 1 and an undisturbed laminar flow pattern were considered. Mixing times of 100–300 ms were measured for a single stage of the mixer. They predicted that the implementation of their improvements in the design of micromixers will result in mixing times of a few milliseconds.

Bertsch et al. [51] investigated computationally mixing in pipes with dimensions on the order of millimeters. They used the commercial code Fluent 5.0 to obtain computational data for water flow at the Reynolds number of 12. They tested two pipes with different types of inserted elements in each one: intersecting channels and right- and left-handed helix elements. In the micromixer made of intersecting channels, the mixer elements split and rearrange the flow and a relatively good dispersion of particles is achieved after only two or three mixing elements. In the case of the mixer made of helical elements, the flow is stretched and folded in each successive element however obtaining a high mixing efficiency requires a large number of elements. Based on the divergence of path lines which enter very close at the inlet, they concluded that their geometries can result in relatively good mixing.

Yi and Bau [52] studied theoretically and computationally the effects of L shaped bends on the mixing of steady, laminar, incompressible flows through a sequence of microconduits with rectangular cross-sections. They showed that at very low Reynolds numbers, flow induced by a single bend does not ensure efficient mixing and a fairly large number of bends are likely to be required to achieve desired mixing effects.

Laminar mixing of gaseous flows in T configuration micromixers with length scales of the order of  $100\ \mu\text{m}$  was studied computationally by Gobby et al. [53]. They developed a model based on the Knudsen number to take into account the effects of slip on wall

boundaries. The effects of different geometrical parameters of the mixer on mixing were shown although no comparison with other models or experimental investigation was reported. Recently, Johnson et al. [54] studied mixing experimentally and computationally in a T microchannel with a series of slanted wells at the junction to generate lateral transport within the channel. The mechanism of slanted wells is to split streams and achieve fast mixing. Their micromixer performed well at low flow rates (0.06 cm/s) for different types of wells. However, at high flow rates (0.81 cm/s), mixing rate depended on the configuration of wells. To investigate the effects of disruption on the mixing of two fluids in microchannels, Wang et al. [55] placed some obstacles in a Y microchannel. Based on their computational studies, the layout and number of obstacles have positive effects on micromixing.

## 2.3 Chaotic Mixing

It is worthwhile to briefly describe chaotic dynamical systems before reviewing the literature of chaotic mixing. Principally, the three main characteristics of a chaotic dynamical systems are: (1) Determinism; (2) Nonlinearity; and (3) Sensitivity.

Determinism means that there are no random terms in the governing equations of the system. In fact, randomness is in sharp contrast to determinism [56–59]. By determinism, an event is caused by certain conditions that cannot possibly lead to any other outcome. For a dynamic situation this means that given the initial conditions, evolution of a system is differentiable and the trajectories can be calculated with reasonable precision. Stated differently, data describing a deterministic phenomenon can be calculated with the use of explicit mathematical formulas. In contrast, the randomness means the input and output forces are not distinguishable explicitly and so only statistical measures of the variable must be considered to establish the nature of the data [60]. For a truly random system, there must be no relationship, even occasionally,

between an observation at the present time, a past observation, or an observation at a future time [58].

A small effect on a system can have significant consequences; conversely, a major effort might yield very little changes. Mathematicians name such events nonlinear [58]. In other words, nonlinearity is the property of a mathematical operation for which the output is not linearly proportional to the input. Usually complexity involves nonlinearity. However, there are no general solutions to nonlinear differential equations, like the full Navier Stokes equations, and such cases must be solved numerically. In any case, nonlinearity is neither desirable nor undesirable. Consider the classical problem of turbulence which is still one of the unsolved problems of physics.

If a slight change in a system can significantly alter the system dynamics, resulting in seemingly unpredictable behavior, it is said the system is sensitive. In terms of differential equations, sensitivity depends on conditions to which equations are exposed, namely, initial and/or boundary conditions [61]. Under very small changes in conditions, solutions of a sensitive differential equation diverge from each other exponentially. However, it should be emphasized that determinism, nonlinearity, and sensitivity are necessary but not sufficient conditions for a dynamical system to be chaotic. Also, note that not all complex systems are chaotic.

The level of chaos of a system depends on the character of the system, its environment, and the nature of their interactions. This level is characterized generally by calculating Lyapunov exponents, as the numerical technique, and mapping Poincaré sections, as the geometrical technique [62, 63].

The existence of chaotic solutions has had a profound effect on thinking in many disciplines. At the present it is believed that chaos can occur in three different systems: (a) conservative (Hamiltonian) systems that experience no energy losses; (b) dissipative systems which are involved with losses; and (c) quantum systems. Practically, the extents of chaotic dynamical systems have been investigated from molecular dynamics [64]

to celestial mechanics [65–68].

Chaotic mixing, introduced and principally developed by Aref [6, 69] and Ottino [48], has raised a new realm for researchers. To date, extensive theoretical, computational, and experimental studies on chaotic mixing have demonstrated the significant advantages of chaos in mixing phenomenon.

Aref [6] was the first person who introduced the concept of chaotic advection and chaotic mixing. He showed computationally that time-periodic flows induced by two stationary blinking vortices in a two-dimensional region can cause chaos and as a result, enhance mixing. The study of chaotic flows actuated by vortices has been continued and developed significantly by Aref et al. [70–73].

Jones et al. [74] studied advection of three-dimensional, steady, laminar, incompressible flows through a sequence of twisted pipe bends of circular cross-section. This twisted pipe consists of curved pipe segments that are not all in the same plane. It was shown that in each segment of pipe, the transverse flow consists of a pair of counter-rotating vortices which can create chaotic particle motions in the cross-stream direction. It was proved that without requiring any additional energy input to the system, stirring can enhance significantly in this pipe due to chaotic advection. Poincaré sections, well-known diagnostic method of dynamical systems, was used to depict chaotic advection. Also, stable and unstable fixed points of the system and then stable and unstable manifolds of these points have been found and illustrated. It has been shown that considerable longitudinal dispersion of a non-diffusing scalar can be produced by the coupling between a chaotic transverse flow and the longitudinal flow. It was concluded that even with a simple geometry, one can capture the essential features necessary to produce efficient stirring in a steady, three-dimensional, laminar flow.

Extensive investigations by Ottino [48, 75] have revealed how chaotic behavior can actually be used to produce beneficial applications in fluid mechanics and mixing. Based on his investigations, chaotic behaviors happen after an oscillatory and before a tran-

sition state to turbulence. A number of active and passive mixers were examined; the common feature is that a periodic behavior in time and/or space is produced by these chaotic mixers. In spatially periodic mixers [76], the geometry of the device is altered to achieve chaotic mixing while in time-periodic mixers, such as flow between two eccentric rotating cylinders [77, 78], usually oscillatory boundary conditions are applied to generate rapid mixing (also refer to [79–83]). Using the concept of periodicity and ergodic theory, D’Alessandro et al. [84, 85] determined the sequence of actions on fluid flows that maximizes entropy and thus mixing. They applied their theory to eggbeater flows first introduced by Ottino [48] and measured the randomness induced by a transformation. They showed that when maximum entropy is satisfied by a periodic sequence of actions, the process of mixing is done faster and the phase space gets homogeneously mixed.

Miles et al. [86] studied the chaotic mixing of Newtonian fluids in a three-dimensional cylindrical cavity numerically and experimentally by means of phase-space trajectories, return maps, and Lyapunov exponents. The upper and lower circular disks of cylinder were rotated while the lateral boundary was stationary. Chaotic mixing was initiated simply by rotating the disks alternately. Due to three-dimensionality and unsteadiness of the flow, homoclinic orbits which exist in a chaotic system were initiated rapidly and caused efficient mixing. Applying the concept of unsteady three-dimensional flows, Cartwright et al. [87] investigated chaotic advection in three-dimensional unsteady incompressible laminar spherical Couette flow. The transition state from non-chaotic to chaotic motions in fluid flows was examined and showed by Poincaré maps in their study.

Bryden and Brenner [8] addressed one of the practical applications of laminar chaos with a computational investigation. By combining two three-dimensional flows, chaotic translation of a spherical drop through a shear flow with buoyancy was considered. The effects of the variation of three non-dimensional parameters such as droplet/bulk fluid viscosity ratio and the relative angle between the shear and translational flows were examined. It was shown that when the ratio of the droplet viscosity to the external-

fluid viscosity increases, the possibility of the onset of chaotic flow decreases. Also, it was illustrated that when the the relative angle between the shear and translational flow is fixed at 45 degrees, considerable chaotic behavior is achieved. These findings were furnished by using Poincaré sections method. Also, it was depicted that mass-transfer processes in chaotic flow fields are significantly enhanced.

However, Rothstein et al. [88] pointed out the possibility of a very important phenomenon occurring in chaotic mixing. It was discussed that the first stages of chaotic mixing are crucial and one must consider and examine what will be happening in the first steps. The associated problem is that chaotic advection of a fluid can cause an initially inhomogeneous impurity for the development of complex spatial structures as the elements of fluid are stretching and folding, even if a time-periodic velocity field exists in the system.

## 2.4 Chaotic Micromixers

Due to the promising effects of chaos in mixing, particularly at very low Reynolds numbers, investigators have examined different means to initiate chaotic behaviors in micromixers. Lee et al. [89, 90] investigated experimentally efficient fluid and particle mixing in two active microdevices. They applied unsteady hydrodynamic pressure perturbations and time-dependent dielectrophoretic forces separately as tools to produce chaotic behavior in the system. In the first case, adjacent channels were sources of the pressure perturbation to generate an unsteady pressure drop and therefore a time-dependent flow, transversely to the main stream. To examine whether chaos does truly occur, they calculated the Lyapunov exponent which was a positive number (0.1). By adding an additional side channel, the Lyapunov exponent equal to 0.4 was reported. In the second case, charged particles were forced by an electric field periodically. Stretching and folding were developed, although not significantly, as the case. The disadvantage

of their micromixers is that there are many moving parts in the system which makes it very difficult to operate the micromixer.

The idea of a biofluidics micromixer based on a pulsed source-sink system, first introduced by Jones and Aref [91] to enhance macromixing by chaotic advection, was employed by Lee et al. [89]. The device, unfortunately, not only has several moving parts but also sustains high pressure that cause problems for manufacturing and reliability of operation.

In an experimental study, Liu et al. [9] applied the idea of three-dimensional chaotic flows, first introduced by Jones et al. [74], to fabricate a chaotic micromixer. Basically, they changed the characteristics of flow from two dimensions to three dimensions by altering a square-wave microchannel into a serpentine microchannel in order to achieve more deformation of the interface between different streams. They compared mixing rates of the square-wave and serpentine microchannels to their results with mixing in a straight microchannel. They performed experiments using two streams of ethyl alcohol with phenolphthalein and sodium hydroxide as indicators for Reynolds numbers ranging between 6 and 70. It was shown that mixing rates in the serpentine channel are considerably higher than the straight and square-wave microchannels. Also, larger mixing rates have been achieved by increasing Reynolds numbers in square-wave and serpentine microchannels. However, in the straight microchannel, lower Reynolds numbers have resulted in higher mixing rates which was due to the larger residence time of streams. It was concluded that the higher mixing rate in a serpentine microchannel is consistent with the occurrence of chaotic advection. Although the mixing of water and alcohol, which have two different densities, has been examined in this study, density variations at different cross sections have not been measured, probably due to the difficulties involved with experimental techniques. Furthermore, based on an experimental study performed by Koch et al. [92], phenolphthalein does not show any visible difference in color depending on the proportion of the two fluids. In other words, the color of phenolphthalein

changes at a certain pH value independent of the mixing ratio of indicator and base.

Stroock et al. [93] fabricated a passive mixer for steady pressure-driven flows in microchannels for Reynolds numbers less than 100. In order to produce transverse components of flow that stretch and fold fluid over the cross section of microchannel, they placed ridges on the microchannel floor. They showed that the minimum length of their microchannel in order to achieve good mixing is less than a simple microchannel with no ridge on the floor. This microchannel offers a simple low-cost solution to the problem of mixing in microfluidics.

Recently, Niu and Lee [94] designed a chaotic active mixer. Multiple-side microchannels were connected to the main microchannel and fluids were pumped through the side microchannels to the main one. They found that the amplitude and frequency of pumped fluids characterize the rate of mixing. However, the disadvantage of this micromixer as other active micromixers is in the difficulty to effectively operate and control the device.

Stremler et al. [10] and Beebe et al. [95] suggested a modification to the serpentine channel of Liu et al. [9] to improve mixing rate even more. The work presented in this thesis is to provide computational data to compare with experimental data obtained by Liu et al. [9] and compare the results with the suggested model of Stremler et al. [10] and Beebe et al. [95].

## CHAPTER 3 PHYSICAL MODEL, GOVERNING EQUATIONS, AND NUMERICAL FORMULATION

The objective of this chapter is to provide an overview of the physical model for the multiphase flow and the corresponding governing equations which were employed to simulate flows of the present work. This model has been incorporated by Fluent Inc. in the commercial software Fluent 6.0. The methodologies used by Fluent for the discretization of the corresponding governing equations are introduced briefly. It must be mentioned that most of the material presented in this chapter have been collected from the manual of Fluent 6.0 [96].

### 3.1 The Mixture Model

Many natural and industrial flows are the mixture of phases. Generally, these flows are named multiphase flows. The concept of phase in multiphase flows is defined basically as an identifiable class of material that interacts with the flow. From the macroscopic description of matter, it is well known that matter can be categorized into four phases (or states): solid, liquid, gas, and plasma (ionized gas) [97]. Except for the solid state, matter in the other three states may be deformed without applying any force, provided that the change of shape takes place over a sufficiently long time. However, the most common types of multiphase flow consist of two phases of the four, e.g. solid-gas, liquid-gas, and liquid-liquid flows.

The mixture model, incorporated in the Fluent software, can be used to simulate the

interaction between two (or more) phases when local equilibrium over short spatial length scales exists. In this model, an Euler-Euler approach is used to simulate the interaction between different phases. The fundamental assumption made is that different phases are treated mathematically as interpenetrating continua which implies that the volume of a phase cannot be occupied by the other phases, leading to the concept of volume fraction. The volume fraction is assumed to be a continuous function of time and space. In addition, the volume fractions for a control volume can be equal to any value between 0 and 1 depending on the space occupied by each phase, however, their summation equals unity. In the mixture model, conservation equations for each phase are derived to obtain one set of equations with similar structures for all phases.

One of the applications of the mixture model is in homogeneous miscible liquid-liquid flows in which a very strong coupling between phases exists and relative velocities of different phases are zero. These characteristics are due to the fact that equilibrium interfacial tension between miscible liquids does not exist [98,99]. Furthermore, the mixture model is proper to model mixing when the volume fractions of mixed phases exceed 10% and in fact phases are quite interpenetrating. These features are very important for the research herein whereby two phases, water and liquid alcohol, will be considered.

Water and liquid alcohol are quite miscible. Zero relative velocities between water and alcohol is a realistic assumption in terms of their interaction when mixing. Furthermore, there is a wide distribution of the dispersed phases of these two completely miscible liquids.

It is worth noting that the mixture model requires less computational effort since fewer equations are solved. Thus, the mixture model is preferable for three-dimensional simulations and enables higher resolution simulations. In addition, the mixture model is more stable than the other multiphase flow models, another advantage to select this model.

## 3.2 Governing Equations

The mixture model can simulate multiple phases by solving the continuity, momentum, and energy equations for the mixture, the volume fraction equations for the secondary phases, and algebraic expressions for the relative velocities. However, only the continuity, momentum, and the volume fraction equations are applied in the simulations of the present work since temperature effects and relative velocities of different phases are absent.

The continuity equation for the mixture of fluids is:

$$\frac{\partial}{\partial t}(\rho_m) + \nabla \cdot (\rho_m \vec{v}_m) = 0 \quad (3.1)$$

where  $t$  is time,  $\rho_m$  is the mixture density, and  $\vec{v}_m$  is the mass-averaged velocity. The mixture density,  $\rho_m$ , is defined as:

$$\rho_m = \sum_{k=1}^n \alpha_k \rho_k \quad (3.2)$$

where  $n$  is the number of phases and  $\alpha_k$  is the volume fraction of phase  $k$ . The mass-averaged velocity,  $\vec{v}_m$ , in Eq. 3.1 is defined as:

$$\vec{v}_m = \frac{\sum_{k=1}^n \alpha_k \rho_k \vec{v}_k}{\rho_m} \quad (3.3)$$

Note that the Schmidt number, which is the ratio of the kinematic viscosity to the diffusion coefficient, was assumed to be infinite. This is an acceptable assumption since the residence time is very small in microfluidics and therefore, the diffusive flux is negligible.

The momentum equation for the mixture can be expressed as:

$$\frac{\partial}{\partial t}(\rho_m \vec{v}_m) + \nabla \cdot (\rho_m \vec{v}_m \vec{v}_m) = -\nabla p + \nabla \cdot \left[ \mu_m (\nabla \vec{v}_m + \nabla \vec{v}_m^T) \right] + \rho_m \vec{g} \quad (3.4)$$

where  $p$  is pressure,  $\mu_m$  is the viscosity of the mixture, and  $\vec{g}$  is the gravitational acceleration. Although buoyancy effects are small owing to the small length scales, it is considered in the performed simulations to obtain realistic results. The viscosity of the mixture,  $\mu_m$ , in Eq. 3.4 is defined as:

$$\mu_m = \sum_{k=1}^n \alpha_k \mu_k \quad (3.5)$$

The volume fraction equation for the secondary phase  $p_2$  can be obtained from the continuity equation for the second phase as:

$$\frac{\partial}{\partial t}(\alpha_{p_2} \rho_{p_2}) + \nabla \cdot (\alpha_{p_2} \rho_{p_2} \vec{v}_m) = 0 \quad (3.6)$$

### 3.3 Numerical Formulation

A finite volume method has been used to discretize the governing equations in Fluent 6.0. The finite volume method consists of integrating the governing equations about each control volume (grid cell), therefore, yielding discrete equations that conserve each quantity on a control-volume basis. Consider the steady-state conservation equation for the transport of a scalar quantity  $\phi$  in an integral form for an arbitrary control volume  $V$ :

$$\oint \rho \phi \vec{v} \cdot d\vec{A} = \oint \Gamma_\phi \nabla \phi \cdot d\vec{A} + \int_V S_\phi dV \quad (3.7)$$

where  $\rho$  is density,  $\vec{v}$  is the velocity vector,  $\vec{A}$  is the surface area vector,  $\Gamma_\phi$  is the diffusion coefficient of scalar  $\phi$ ,  $\nabla$  is the gradient, and  $S_\phi$  is the source of scalar  $\phi$  per unit volume. The discretization of Eq. 3.7 for a control volume, shown in Fig. 3.1, results in:

$$\sum_f^{N_{faces}} \rho_f \vec{v}_f \phi_f \vec{A}_f = \sum_f^{N_{faces}} \Gamma_\phi (\nabla \phi)_n \vec{A}_f + S_\phi V \quad (3.8)$$

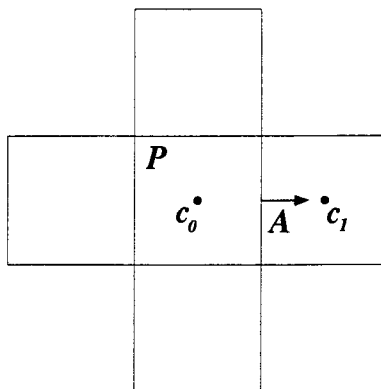


Figure 3.1 Control volume used to illustrate discretization of a scalar transport equation.

where  $N_{faces}$  is the number of faces enclosing the cell,  $\phi_f$  is the scalar  $\phi$  convected through face  $f$ ,  $\vec{A}_f$  is the area of face  $f$ ,  $\rho_f \vec{v}_f \vec{A}_f$  is the mass flux through the face  $f$ ,  $(\nabla\phi)_n$  is the magnitude of  $\nabla\phi$  normal to face  $f$ , and  $V$  is the cell volume. The equations solved by Fluent take the same general form as the one given by Eq. 3.8 and are applied readily to the mesh.

It is worth mentioning that in Fluent software, the discrete values of the scalar  $\phi$  are stored at the cell centers ( $c_0$  and  $c_1$  in Fig. 3.1). However, to solve the convection terms in Eq. 3.8, face values  $\phi_f$  are required. This is accomplished using interpolation schemes which calculate the required data from the cell center values.

### 3.3.1 Segregated solver

A segregated approach (pressure correction approach) with an implicit formulation was chosen to solve for the governing equations. Since a steady-state calculation is desired, the time-dependent terms of governing equations (Eqs. 3.1, 3.4 and 3.6) are dropped. Therefore, the general integral form of steady-state continuity and momentum equations are:

$$\oint \rho \vec{v} \cdot d\vec{A} = 0 \quad (3.9)$$

$$\oint \rho \vec{v} \cdot d\vec{A} = - \oint p I \cdot d\vec{A} + \oint \bar{\tau} \cdot d\vec{A} + \int_V \vec{F} dV \quad (3.10)$$

where  $I$  is the identity matrix,  $\bar{\tau}$  is the stress tensor, and  $\vec{F}$  is the force vector.

The discretized form of the continuity equation (Eq. 3.9) can be obtained by integrating over the control volume shown in Fig. 3.1:

$$\sum_f^{N_{faces}} J_f A_f = 0 \quad (3.11)$$

where  $J_f$  is the mass flux  $\rho v_n$  through face  $f$ . The face flux,  $J_f$ , is written as:

$$J_f = \hat{J}_f + d_f (p_{c_0} - p_{c_1}) \quad (3.12)$$

where  $p_{c_0}$  and  $p_{c_1}$  are the pressures within the two cells on either side of the face, and  $\hat{J}_f$  contains the influence of velocities in these cells. Since the term  $d_f$  is related to the discretized form of the momentum equation, it is defined later.

The procedure outlined for the scalar transport is used to discretize the momentum equations. For instance, the  $x$ -momentum equation can be obtained by setting  $\phi = u$  as:

$$a_P u = \sum_{nb} a_{nb} u_{nb} + \sum p_f A \cdot \hat{i} + S \quad (3.13)$$

where subscripts  $P$  and  $nb$  stand for the cell and its neighboring cells, respectively. The coefficient  $a_P$  is a weighting factor. This coefficient is applied to relate the face values of velocity,  $\vec{v}_n$ , to stored values of velocity at the cell center. The method is typically called momentum-weighted averaging. Finally, the term  $d_f$  in Eq. 3.12 is a function of  $\bar{a}_P$ , the average of the  $a_P$  coefficients for the cells on either side of face  $f$ .

In Fluent the values of pressure and velocity are stored at cell centers while in Eq. 3.13 the values of the pressure at the face between cells  $c_0$  and  $c_1$ , shown in Fig. 3.1 are

required. Fluent uses different interpolating schemes to calculate the face values of pressure from the cell values.

### 3.3.2 Second-order upwind scheme

To obtain more accurate results, a second-order upwind scheme was selected for discretization of the momentum and volume fraction equations. In an upwind scheme, face values are derived from quantities in the cell upstream, relative to the direction of the normal velocity. In this scheme, quantities at cell faces are computed using a multi-dimensional linear reconstruction approach. By this approach, higher-order accuracy is obtained at cell faces using Taylor series expansions of the cell-centered solution about the cell centroid. Thus, when second-order upwind scheme is applied, the face value  $\phi_f$  is calculated using the following expression:

$$\phi_f = \phi + \nabla\phi \cdot \Delta\vec{s} \quad (3.14)$$

where  $\phi$  and  $\nabla\phi$  are the cell-centered value and its gradient in the upstream cell, respectively, and  $\Delta\vec{s}$  is the displacement vector from the upstream cell centroid to the face centroid. The gradient  $\nabla\phi$  in each cell is computed using the divergence theorem as:

$$\nabla\phi = \frac{1}{V} \sum_f^{N_{faces}} \phi_f \vec{A} \quad (3.15)$$

Here the face values  $\phi_f$  are calculated by averaging  $\phi$  from the two cells adjacent to the face. Finally, the gradient  $\nabla\phi$  is limited so no new maxima or minima are introduced in the solution.

### 3.3.3 Central-difference scheme

The diffusion terms in Eq. 3.8 are discretized using a second-order central-difference method. This scheme calculates the face values for a variable ( $\phi_f$ ) as follows:

$$\phi_{f,CD} = \frac{1}{2} (\phi_0 + \phi_1) + \frac{1}{2} (\nabla\phi_{r,0} \cdot \vec{r}_0 + \nabla\phi_{r,1} \cdot \vec{r}_1) \quad (3.16)$$

where the indices 0 and 1 refer to the cells that share face  $f$ ,  $\nabla\phi_{r,0}$  and  $\nabla\phi_{r,1}$  are the reconstructed gradients at cells  $c_0$  and  $c_1$ , respectively, and  $\vec{r}$  is the vector directed from the cell centroid towards the face centroid.

It is well known that the central-difference scheme can produce unbounded solutions and non-physical oscillations which can lead to instabilities in the numerical procedure [100]. These instability problems can often be avoided if a deferred approach is used for the central-difference scheme. In this approach, the face value is calculated as follows:

$$\phi_f = \phi_{f,UP} + (\phi_{f,CD} - \phi_{f,UP}) \quad (3.17)$$

where  $UP$  stands for upwind. In Eq. 3.17,  $\phi_{f,UP}$  and  $(\phi_{f,CD} - \phi_{f,UP})$  are implicit and explicit parts of the procedure, respectively. As indicated, the upwind part is treated implicitly while the difference between the central-difference and upwind values is treated explicitly. When the numerical solution converges, this approach leads to pure second-order differencing.

### 3.3.4 Under-relaxation factors

Since the governing equations are nonlinear, it is necessary to control the change of scalar variable  $\phi$ . For this reason, an under-relaxation technique has been implemented into Fluent. Basically, this technique decreases the change of scalar  $\phi$  generated at each iteration as:

$$\phi = \phi_{old} + \eta \Delta\phi \quad (3.18)$$

Based on Eq. 3.18, the new value of  $\phi$  depends on the old value  $\phi_{old}$ , the computed change of  $\Delta\phi$ , and the under-relaxation factor,  $\eta$ . The recommended under-relaxation

factors for the mixture model (assuming negligible diffusion) are 0.3, 0.7, and 0.2 for pressure, momentum, and volume fraction, respectively [96]. For density and body forces the under-relaxation was set to 1.

### 3.3.5 SIMPLE method

To effectively control the coupling between pressure and velocity fields, the SIMPLE method was chosen. The SIMPLE method is based on a cyclic series of guessed-and-corrected operations to solve the governing equations [101]. First the velocity field is computed from the momentum equations by guessing the pressure field. Then, the pressures and velocities are corrected to satisfy the continuity equation. By repeating this procedure, the solution is obtained when convergence is satisfied.

If the momentum equation is solved with a guessed pressure field  $p^*$ , the resulting face flux,  $J_f^*$ , computed from Eq. 3.12:

$$J_f^* = \hat{J}_f^* + d_f(p_{c_0}^* - p_{c_1}^*) \quad (3.19)$$

does not satisfy the continuity equation. Consequently, a correction  $J'_f$  is added to the face flux  $J_f^*$  so that the corrected face flux,  $J_f$

$$J_f = J_f^* + J'_f \quad (3.20)$$

satisfies the continuity equation. The SIMPLE algorithm postulates that  $J'_f$  be written as:

$$J'_f = d_f(p'_{c_0} - p'_{c_1}) \quad (3.21)$$

where  $p'$  is the cell pressure correction. The SIMPLE method substitutes the flux correction Eqs. 3.20 and 3.21 into the discretized continuity equation (Eq. 3.11).

### 3.3.6 Residuals in segregated solver

Following discretization using the segregated solver, the conservation equation for a variable  $\phi$  at the cell  $P$  can be derived as:

$$a_P \phi_P = \sum_{nb} a_{nb} \phi_{nb} + b \quad (3.22)$$

where  $a_P$  is the center coefficient,  $a_{nb}$  are the influence coefficients of the neighboring cells, and  $b$  is the contribution of the boundary conditions and the constant part of the source term  $S_c$  in  $S = S_c + S_P \phi$ . In Eq. 3.22, the center coefficient,  $a_P$  is defined as:

$$a_P = \sum_{nb} a_{nb} - S_P \quad (3.23)$$

Basically, the residual  $R^\phi$  is the imbalance which exists in Eq. 3.22 and summed over all the computational cells  $P$ . It can be written as:

$$R^\phi = \sum_{cells\ P} \left| \sum_{nb} a_{nb} \phi_{nb} + b - a_P \phi_P \right| \quad (3.24)$$

To scale the residuals in Eq. 3.24, a scaling factor as the representative of the flow rate of  $\phi$  is introduced into Eq. 3.24 as:

$$R^\phi = \frac{\sum_{cells\ P} \left| \sum_{nb} a_{nb} \phi_{nb} + b - a_P \phi_P \right|}{\sum_{cells\ P} |a_P \phi_P|} \quad (3.25)$$

For the momentum equations the denominator term  $a_P \phi_P$  is replaced by  $a_P v_P$ , where  $v_P$  is the magnitude of the velocity at cell  $P$ .

The unscaled residual for the continuity equation is defined as:

$$R^c = \sum_{cells\ P} |\text{rate of mass creation in cell } P| \quad (3.26)$$

To scale the continuity residual, the right hand side of Eq. 3.26 is divided by the largest absolute value of the continuity residual in the first five iterations as:

$$\frac{R_{iter\ N}^c}{R_{iter\ 5}^c} \quad (3.27)$$

## CHAPTER 4 STATEMENT OF PROBLEM AND COMPUTATIONAL CONSIDERATIONS

In this chapter, the statement of the microfluidics problem is described in terms of the geometry, physical properties of selected liquids, and initial and boundary conditions used in the simulations. To examine the sensitivity of solution to grid size, the results of grid resolution tests are presented. Finally, the performance of computational studies are overviewed.

### 4.1 Statement of Problem

#### 4.1.1 Geometry of microchannels

Four types of microchannels were considered to simulate three-dimensional steady-state two-phase flows. Illustrated in Fig. 4.1 are the schematics of these microchannels: (a) straight, (b) square-wave, (c) serpentine, and (d) twisted microchannel. The straight microchannel is shown in Fig. 4.1(a). Obviously, there is no bend in the straight microchannel. This microchannel has the dimensions of 5.1, 0.3, and, 0.15 mm in  $x$ -,  $y$ -, and  $z$ -directions, respectively.

Shown in Fig. 4.1(b) is the square-wave microchannel which was first introduced by Branebjerg et al. [102]. The square-wave microchannel has two consecutive C-shaped bends in the  $x$ - $y$  plane. Each bend consists of five similar blocks. Figure 4.2 depicts the dimensions of each block which are 300, 300, and 150  $\mu\text{m}$  in  $x$ -,  $y$ -, and  $z$ -directions, re-

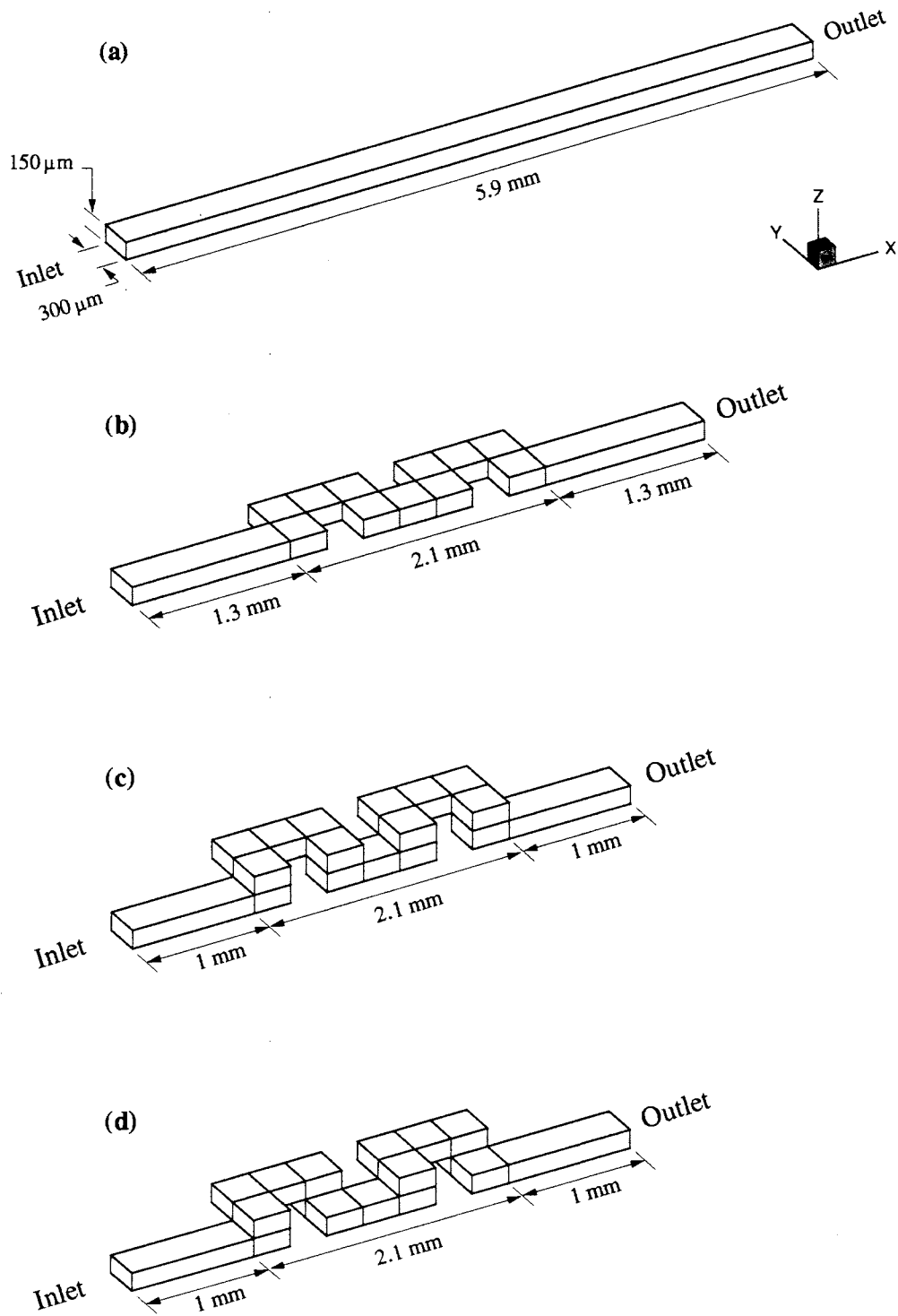


Figure 4.1 Schematic of microchannels: (a) straight, (b) square-wave, (c) serpentine, and (d) twisted microchannel. The distance between inlet and outlet along the centerline is  $5.9\ \text{mm}$  in all microchannels.

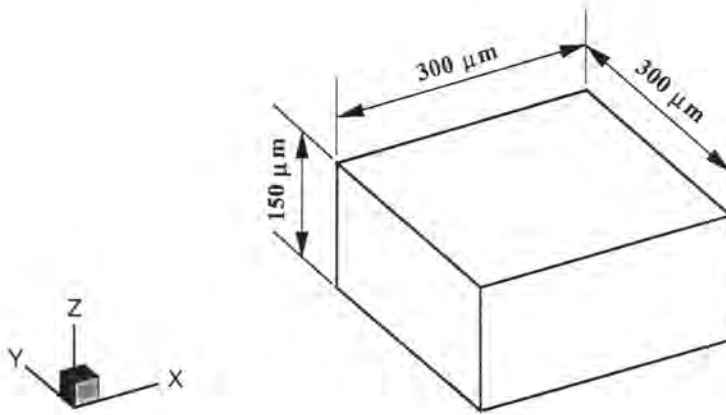


Figure 4.2 Dimensions of each block to build different types of bends in square-wave, serpentine, and twisted microchannels.  $300\ \mu\text{m}$  in  $x$ - and  $y$ -directions and  $150\ \mu\text{m}$  in  $z$ -direction were considered to be consistent with the study of Liu et al. [9].

spectively. Both entrance and exit lengths are 1.3 mm in the square-wave microchannel.

The serpentine microchannel which was introduced and experimentally tested by Liu et al. [9], has been shown in Fig. 4.1(c). Actually, the serpentine microchannel is the modified version of square-wave microchannel. In the serpentine microchannel, the C-shaped bends of the square-wave microchannel have been moved upward ( $z$ -direction) equal to the height of a block ( $150\ \mu\text{m}$ ). Entrance and exit lengths are 1 mm for the serpentine microchannel.

Figure 4.1(d) shows the twisted microchannel, which has been suggested by Stremler et al. [10]. In fact, the twisted microchannel is the modified version of the serpentine microchannel. Entrance and exit lengths are 1 mm in the twisted microchannel. To appreciate the difference between the serpentine and twisted microchannels, as well as the other two microchannels, it is better to look at the direction of the core of flow in these microchannels.

Figure 4.3 illustrates the direction of the core of the flow in four microchannels. It

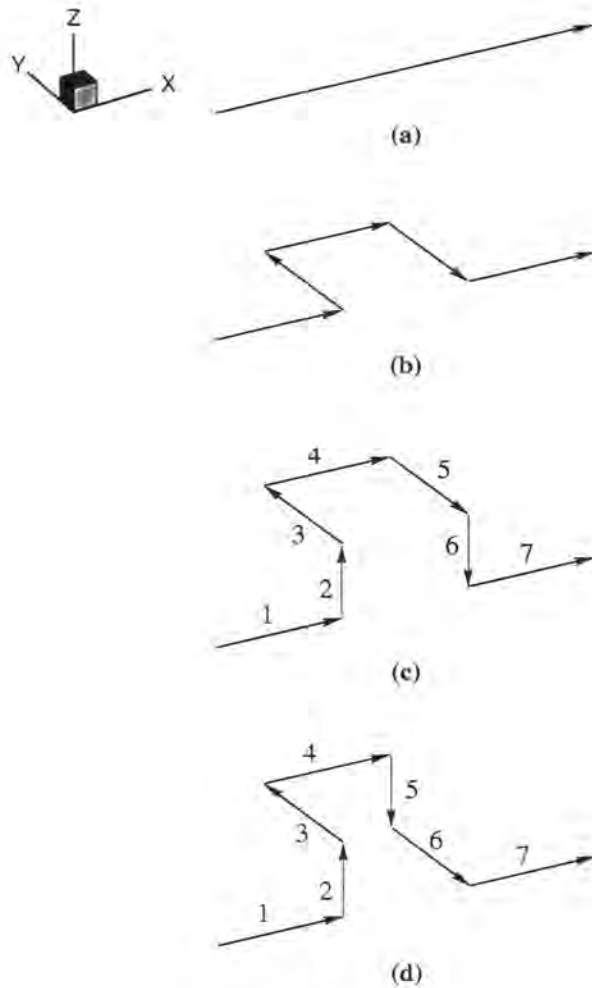


Figure 4.3 Schematic of flow direction in (a) straight, (b) square-wave, (c) serpentine and (d) twisted microchannels.

is obvious, as shown in Fig. 4.3(a), that in the straight microchannel, the core flow moves only in one direction ( $x$ -direction). Having C-shaped bends in the square-wave microchannel, the core flow lies in  $x$ - $y$  plane (Fig. 4.3(b)) albeit the microchannel is three-dimensional. Shown in Fig. 4.3(c) is the evolution of flow in the serpentine microchannel. It can be seen that flow can move in all three dimensions in the serpentine microchannel. However, the consecutive turns are not always perpendicular to the plane of the last two turns. For example, the movement shown by vector 5 is still in the plane constructed by vectors 3 and 4. The twisted microchannel allows the flow to move in all

three directions such that the third turn is perpendicular to the last two turns. It can be observed from Fig. 4.3(d) that all turns are perpendicular to the plane of the last two turns. In fact, the effect of the twisted microchannel on the flow is to “twist” fluids continuously in space and time.

It should be mentioned that at least three out of four degrees of freedom (three degrees for space and one degree for time) are necessary for a flow field to possess chaotic advection [103]. For example, a steady-state flow must be three-dimensional for the onset of chaos. The serpentine and twisted microchannels in which the core of flow is three-dimensional possess this necessary condition.

The four microchannels have two common features. The first feature is that the cross sectional area, also shown in Fig. 4.2, is  $300\ \mu\text{m} \times 150\ \mu\text{m}$  for all microchannels. Consequently, the hydraulic diameter of all these microchannels, defined as the ratio of four times the cross sectional area to the perimeter of the cross section, is  $200\ \mu\text{m}$ . The second feature is that the distance between the inlets and outlets, moving along the centerline, is  $5.9\ \text{mm}$  in all microchannels. This feature makes the mixing comparison amongst each microchannel logical and reasonable.

#### 4.1.2 Physical properties of selected liquids

Water and liquid ethyl alcohol were selected to examine the interaction and mixing of two liquids in the microchannels. These liquids are completely miscible which suits to simulate the mixing of two-fluid flows with the wide distribution of the dispersed phases. The density and viscosity of water are  $1000\ \text{kg}/\text{m}^3$  and  $0.001\ \text{kg}\cdot\text{s}/\text{m}$ , respectively. The density and viscosity of liquid ethyl alcohol are  $800\ \text{kg}/\text{m}^3$  and  $0.0012\ \text{kg}\cdot\text{s}/\text{m}$ , respectively. Consequently, the density of a completely mixed flow of these two liquids is  $900\ \text{kg}/\text{m}^3$  based on Eq. 3.2 and it happens when the volume fraction of each phase is 0.5 in each cell. Also, by considering Eq. 3.5, theoretically the viscosity of a fully mixed flow should be  $0.0011\ \text{kg}\cdot\text{s}/\text{m}$ . The density and viscosity of a fully mixed flow

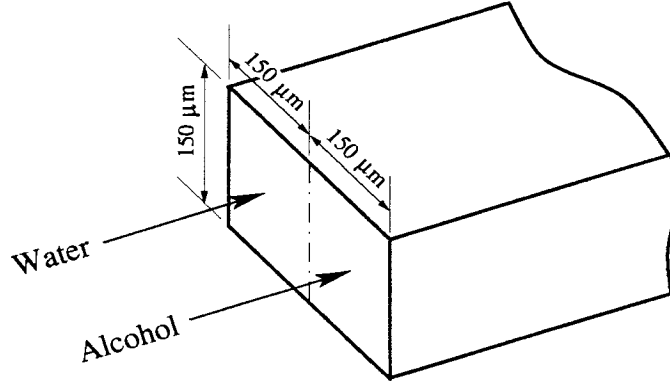


Figure 4.4 Plug flows of water and alcohol side by side as the inlet boundary conditions.

was considered to calculate the Reynolds number.

#### 4.1.3 Initial and boundary conditions

Shown in Fig. 4.4 are boundary conditions at the inlet of the microchannels. Illustrated in this figure are two plug flows of water and alcohol side by side. The velocity of water and alcohol at the inlet was specified so that Reynolds numbers of 6, 12, 35, 70, and 96 were obtained. The Reynolds number is defined as:

$$Re = \frac{\bar{\rho} \bar{U} D_H}{\bar{\mu}} \quad (4.1)$$

where  $\bar{\rho}$  is the density of a fully mixed flow ( $900 \text{ kg/m}^3$ ),  $\bar{U}$  is the average velocity (velocity of water and alcohol at the inlet),  $D_H$  is the hydraulic diameter ( $200 \text{ } \mu\text{m}$ ), and  $\bar{\mu}$  is the viscosity of a fully mixed flow ( $0.0011 \text{ kg}\cdot\text{s/m}$ ).

The no-slip boundary condition on all the walls was imposed. At the outlet, gage pressure equal to zero was specified. Since velocity at the inlet and pressure at the outlet have been selected as boundary conditions, the numerical solution of governing equations is more stable and less difficulties are encountered to capture the converged solution.

To add stability in the early stages of the steady-state calculations, the initial condition for the streamwise velocity was set equal to the inlet velocity in the whole domain including the inlet. The other components of velocity were set to zero. Furthermore, only water was initialized in the domain.

## 4.2 Computational Considerations

### 4.2.1 Grid resolution tests

Once the microchannel geometries were specified, the commercial grid generator Gambit [104] was used to create the grid. Because geometries are based on rectangular blocks, uniform hexahedral cells were used to build the mesh. The aspect ratio of spatial increments in  $x$ -,  $y$ -, and  $z$ -directions with respect to each other was chosen as unity.

To ensure that simulations have not been affected by the grid size significantly, grid resolution tests were carried out. The serpentine microchannel at the Reynolds number of 70 was selected for grid tests. The grid size was determined based on the number of cells in each block shown in Fig. 4.2. Table 4.1 summarizes the number of cells in each block, spatial increments in  $x$ -,  $y$ -, and  $z$ -directions, and the total number of cells for each case.

Generating  $20 \times 20 \times 10$  cells in  $x$ -,  $y$ -, and  $z$ -directions for each block (Fig. 4.2), the first solution was obtained for a total of 86,600 cells. Then, by doubling the number of cells in all three directions, which corresponds to  $40 \times 40 \times 20$  cells in each block, the second solution was attained with 693,600 total number of cells. To compare different

Table 4.1 Mesh sizes used for grid resolution tests.

Grid cells in $x$ , $y$ , and $z$	$\Delta x = \Delta y = \Delta z$ ( $\mu\text{m}$ )	Total number of cells
$20 \times 20 \times 10$	15	86,800
$40 \times 40 \times 20$	7.5	693,600
$50 \times 50 \times 25$	6	1,355,000

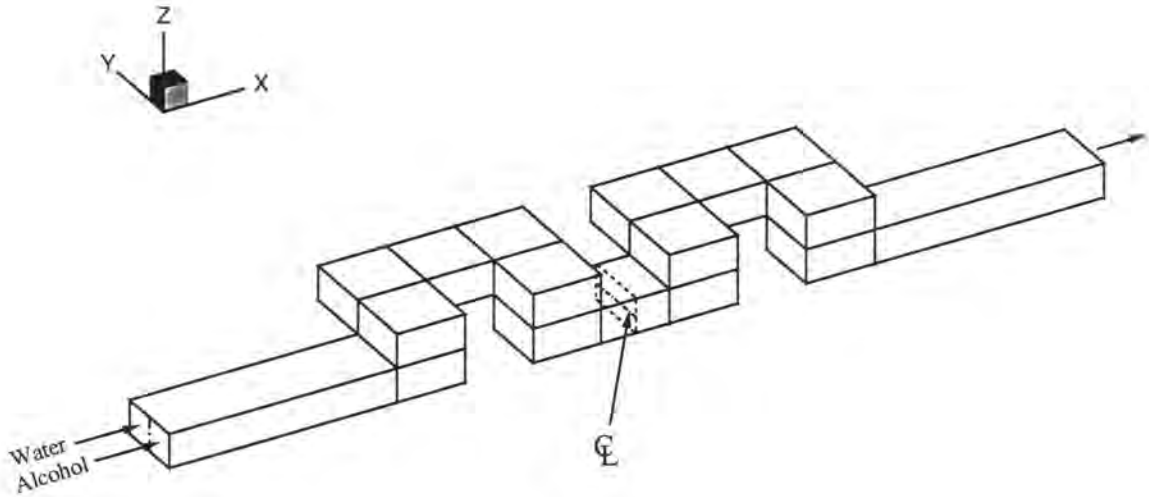


Figure 4.5 Centerline of the mid cross-section of the serpentine microchannel.

solutions, a line on the mid section of the microchannel was specified.

Shown in Fig. 4.5 is the centerline  $\mathcal{C}_L$  of the mid cross section of the serpentine microchannel, the location where solutions were compared. It is worth mentioning that since this location is at the middle of the microchannel, inlet and outlet boundaries have minimal, if any, effects. The variation of the mixture density, as the representative of the most crucial and sensitive variable, was considered for comparison between different grid sizes.

Figure 4.6 shows the mixture density variation along centerline  $\mathcal{C}_L$  for grid sizes of 86,800 (dashed line) and 693,600 (dashed-dot line) cells. To find the amount of error in the solution, a Richardson extrapolation was applied to these two grids. The Richardson extrapolation [105] is expressed as:

$$\text{Better estimate} = \text{more accurate} + \frac{1}{2^n - 1} (\text{more accurate} - \text{less accurate}) \quad (4.2)$$

where  $n$  is the order of accuracy of the solution. In the present work, since second order accurate schemes were used for the discretization of governing equations,  $n$  is

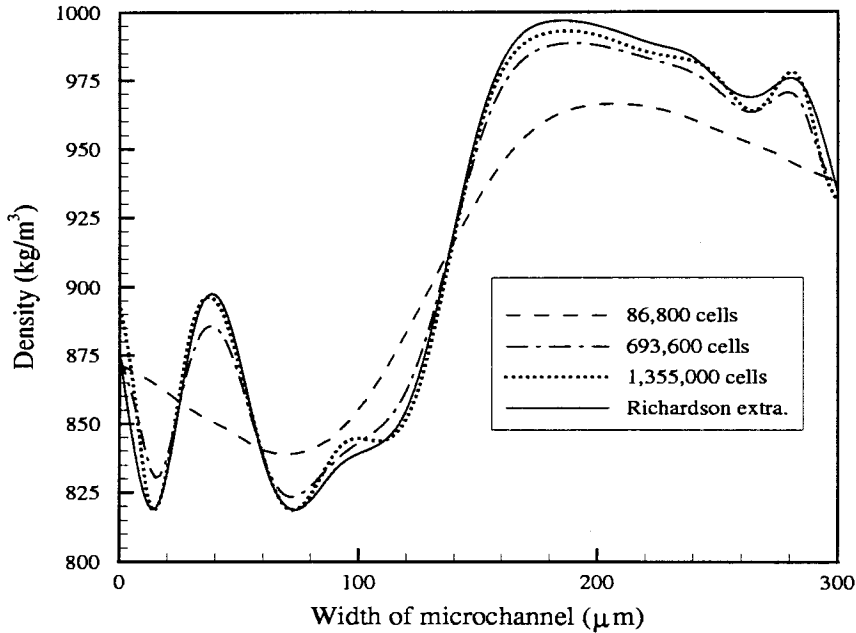


Figure 4.6 Grid resolution test for serpentine microchannel at  $Re=70$  using Richardson extrapolation.

two. Also less accurate and more accurate solutions are the solutions obtained by grid sizes of 86,800 and 693,600 cells in each block, respectively. Applying Eq. 4.2 to these grids, extrapolated data were obtained and plotted (solid line) against other curves. To obtain a better solution, simulations were performed with the grid size of  $50 \times 50 \times 25$  cells in each block, totaling 1,355,000 cells. Results have been demonstrated against extrapolated data in Fig. 4.6 (dotted line). It can be observed that very good agreement exists between the Richardson extrapolated data and the grid size of 1,355,000 cells. In fact, by applying the grid size of 1,355,000 cells, only a maximum error of 2% has been introduced in the solution. Therefore, simulations were performed in conjunction with the grid size of  $50 \times 50 \times 25$  cells in each block (1,355,000 total number of cells).

### 4.2.2 Steady-state calculations

Preliminary numerical studies of the serpentine microchannel for the Reynolds number of 70 indicated that flow is steady. To verify the nature of the flow both transient and steady-state simulations were performed for the serpentine microchannel. It was observed that the transient simulation converged to the steady-state simulation. Likewise, the experimental results in the study of Liu et al. [9] indicated the steady-state nature of flow in the serpentine microchannel. Therefore, steady-state calculations were considered for all the simulations.

### 4.2.3 Computational performance

Parallel computing is a powerful tool in performing computationally expensive three-dimensional simulations. One of the methods of parallel computing, particularly used in computational fluid dynamics, is the domain decomposition method. By this method, each processor computes all the calculations in a particular domain. Then, processors communicate the computed data amongst themselves. This procedure continues until the converged solution is obtained.

Parallel computations were performed using the SGI Origin 2000 of the High Performance Computing Center at Iowa State University. This machine is a virtual shared memory computer configured with node cards [106]. Each node card includes two CPUs, a memory card, and a network interface card. The peak rate of the network communication is 130 MB/s. Each CPU is an MIPS R12000 processor running at 300 MHz, and has separate on-chip 32 KB data and instruction caches, and an 8 MB off-chip unified cache. Each pair of CPUs share 2 GB of memory, yielding the system a total of 16 GB. For shared memory parallel program, off-node memory has to be used if data storage is large, and is slower than on-node memory.

Computational domains were partitioned into eight zones to perform simulations

with eight processors for parallel computations. The convergence criteria was set so that all the residuals decreased at least three orders of magnitude with respect to the residuals at the tenth iteration. Meanwhile, double precision residuals were selected to obtain more accurate results. Having these configurations, approximately 0.0897 millisecond/iteration/cell was required for each simulation.

## CHAPTER 5 RESULTS

To assess the efficiency of microchannel designs (straight, square-wave, serpentine, and twisted), simulations were carried out for five Reynolds numbers ranging between 6 and 96. Results are presented in this chapter in terms of mixing index based on density distribution, contour plots of density, pressure drop, and path lines for the selected Reynolds numbers.

### 5.1 Mixing Index

To measure mixing in each microchannel, three cross sections  $A$ ,  $B$ , and  $C$  were chosen. Figure 5.1 illustrates the locations of these cross sections. Although the shortest distance along the  $x$ -axis between inlet and each section vary in each microchannel, these distances when measured along the centerline are the same for all microchannels. Measuring along the centerline, the distance between inlet and sections  $A$ ,  $B$ , and  $C$  are 0.8, 2.95, and 5.1 mm, respectively, in each of the microchannels. Note that (with the exception of the straight microchannel) section  $A$  is before the first segment, section  $B$  is between the first and second segments, and section  $C$  is after the second segment.

To quantify the mixing index, the deviation of density from the average density value is:

$$\text{Mixing index} = \left( 1 - \frac{\sqrt{\frac{1}{N} \sum_{i=1}^N (\rho_{i,sect} - \bar{\rho})^2}}{\sqrt{\frac{1}{N} \sum_{i=1}^N (\rho_{i,inlet} - \bar{\rho})^2}} \right) \times 100 \quad (5.1)$$

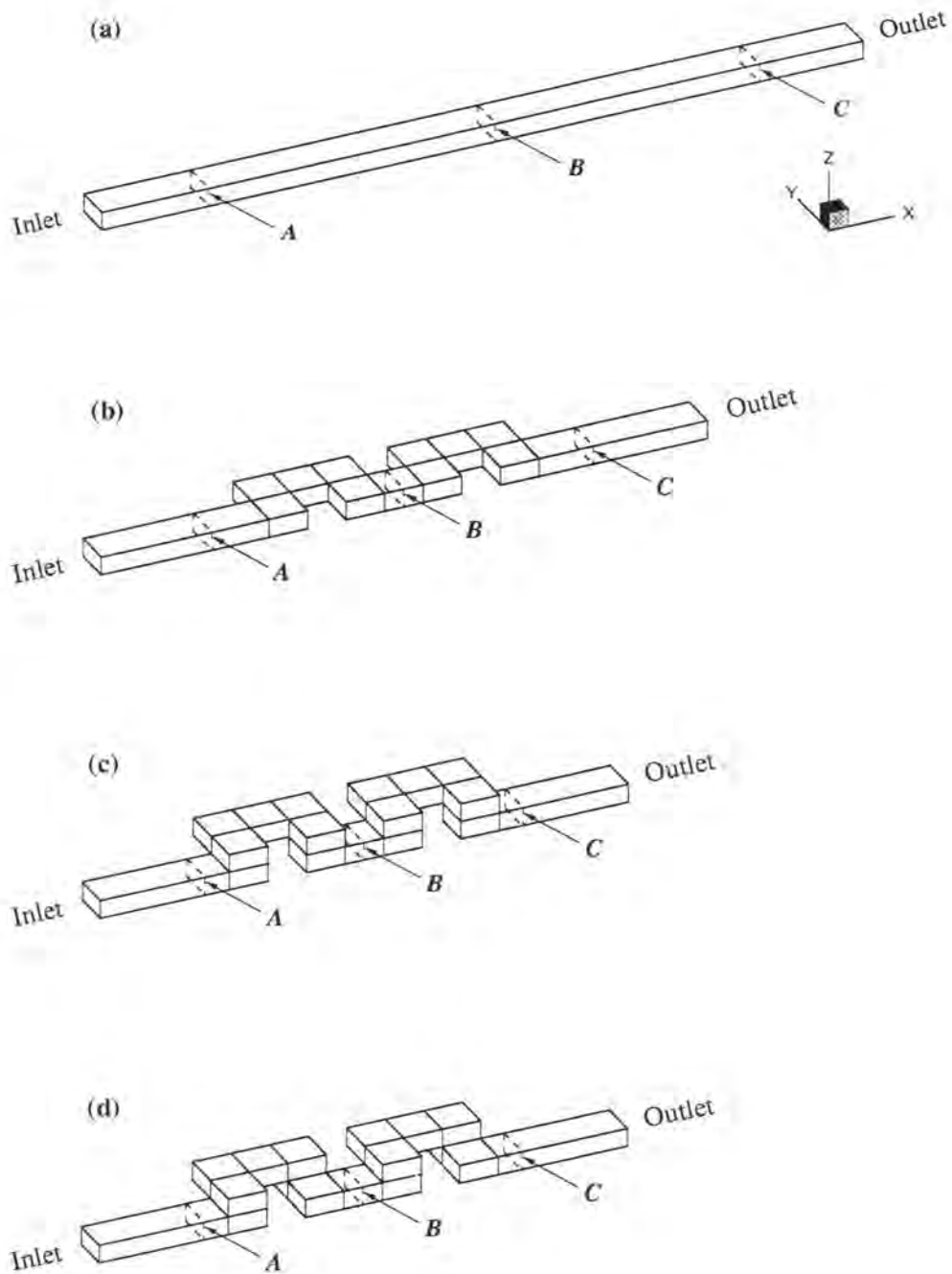


Figure 5.1 The location of cross sections  $A$ ,  $B$ , and  $C$ , where mixing index is quantified, in each microchannel: (a) straight, (b) square-wave, (c) serpentine, and (d) twisted microchannel. The distance between inlet and cross sections  $A$ ,  $B$ , and  $C$  along the centerline are 0.8, 2.95, and 5.1 mm for all microchannels.

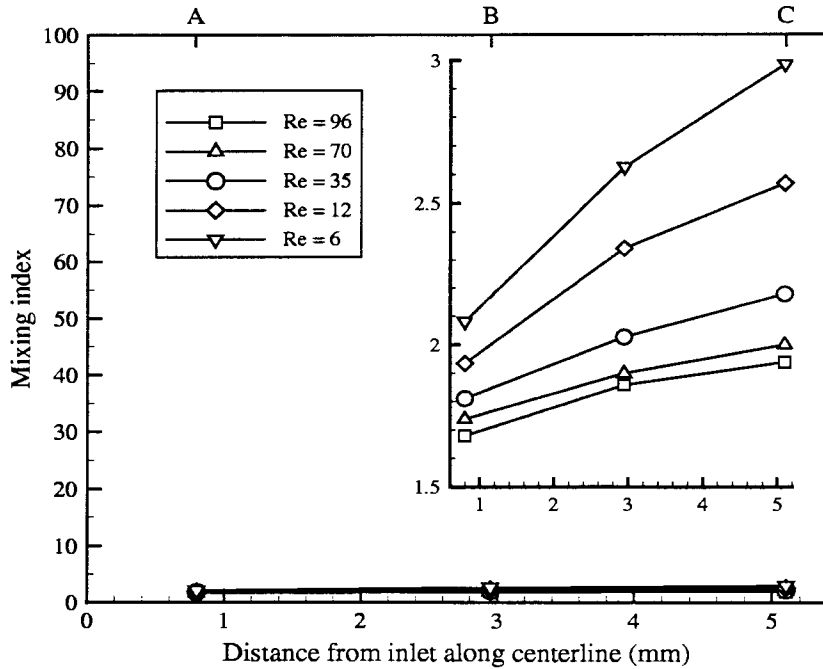


Figure 5.2 Mixing index versus centerline distance in the straight microchannel for various Reynolds numbers.

where  $N$  is the total number of cells at the desired cross section,  $\rho_{i,sect}$  is the density of mixture at the  $i$ th cell on the cross section,  $\bar{\rho}$  is the density of a fully mixed flow defined by Eq. 3.2 ( $900 \text{ kg/m}^3$  in the present work), and  $\rho_{i,inlet}$  is the density of the  $i$ th cell at the inlet. The fraction term in parentheses of Eq. 5.1 is the intensity of segregation. Mathematically, the numerator represents the standard deviation at the desired section. To avoid misinterpretation due to different amplitudes, normalization is applied such that the denominator is the standard deviation at the inlet. Applying Eq. 5.1 for sections  $A$ ,  $B$ , and  $C$ , shown in Fig. 5.1, results were obtained for Reynolds numbers of 6, 12, 35, 70, and 96. Figures 5.2–5.5 display the mixing index in each microchannel.

Shown in Fig. 5.2 is the mixing index versus centerline distance from the inlet in the straight microchannel. It can be observed that mixing is negligible (less than 3) in the straight microchannel even though Reynolds number has been increased by a factor of

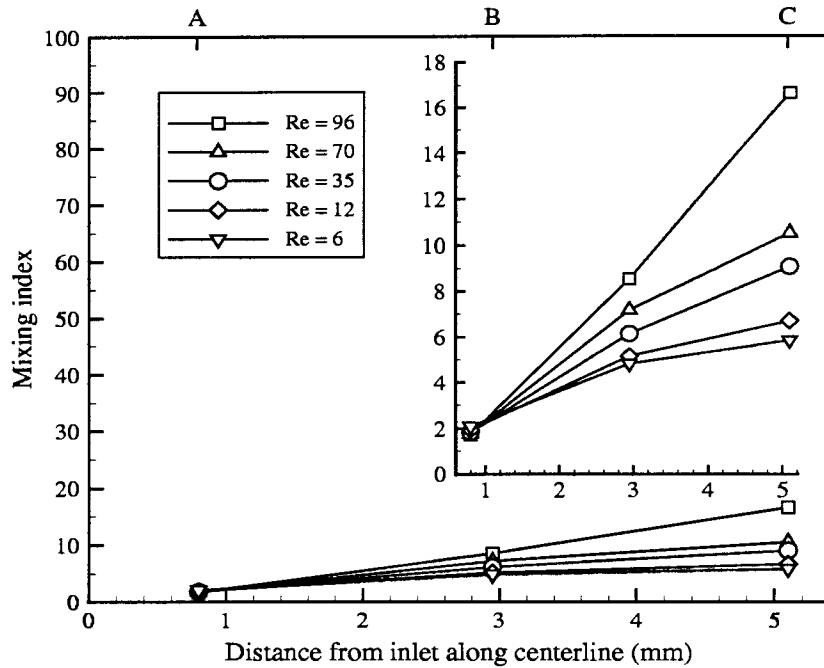


Figure 5.3 Mixing index versus centerline distance in the square-wave microchannel for various Reynolds numbers.

16. Upon closer inspection of the very small range of mixing (1.5–3), decreasing the Reynolds number results in better mixing due to the increase in the residence time of small Reynolds number flows. In fact, there is an inverse relationship between mixing index and Reynolds number in the straight microchannel which is in agreement with the findings of Liu et al. [9].

Figure 5.3 illustrates the mixing index in the square-wave microchannel. It is observed that by increasing the Reynolds number, mixing has generally developed more. In spite of a considerable difference in Reynolds numbers ranging between 6 and 70, the change in the corresponding mixing index is not significant (5–10). However, when Reynolds number is 96, mixing has developed considerably more (17) at section C.

Figure 5.4 demonstrates the variation of mixing in the serpentine microchannel. The trend of mixing in the serpentine microchannel is similar to the square-wave microchannel; increasing the Reynolds number increases the mixing index. However, the serpentine

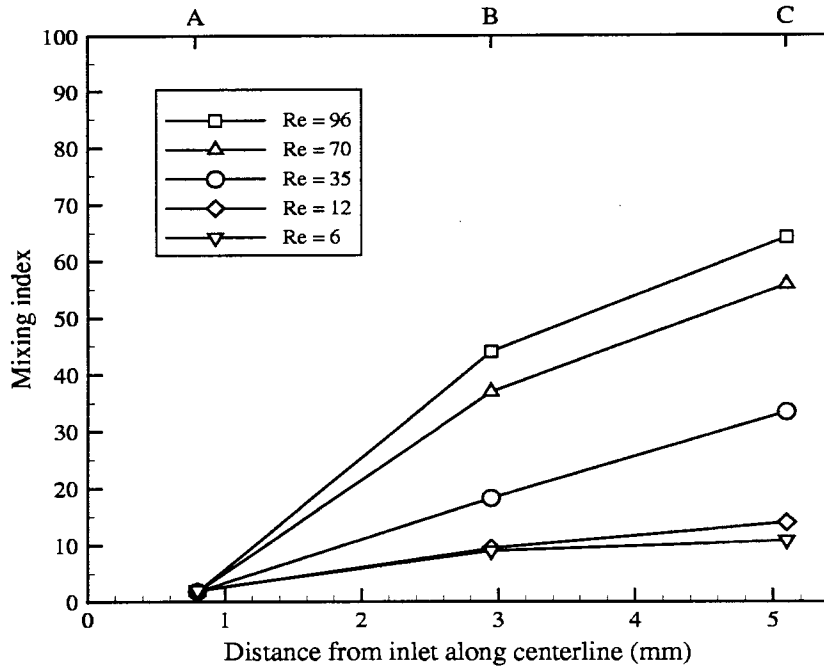


Figure 5.4 Mixing index versus centerline distance in the serpentine microchannel for various Reynolds numbers.

microchannel more effectively increases the mixing index than in the square-wave microchannel. It can be seen that when Reynolds number increases from 6 to 96, the index of mixing increases significantly from 12 to 65.

Illustrated in Fig. 5.5 is the mixing index in the twisted microchannel. The trends are similar to the square-wave and serpentine microchannels; larger Reynolds numbers result in higher mixing indexes. Also, a significant increase in the mixing index can be seen for the Reynolds number of 35 in the twisted microchannel from section *B* to section *C*. In fact, the mixing indexes at section *C* for the Reynolds numbers of 35 and 70 are very close to each other while this behavior was not observed in the serpentine microchannel.

In order to compare the mixing index of each microchannel, the data shown in Figs. 5.2–5.5 is rearranged and presented in Figs. 5.6–5.10 for fixed Reynolds numbers. Figure 5.6 shows the variation of mixing in each microchannel for the Reynolds number

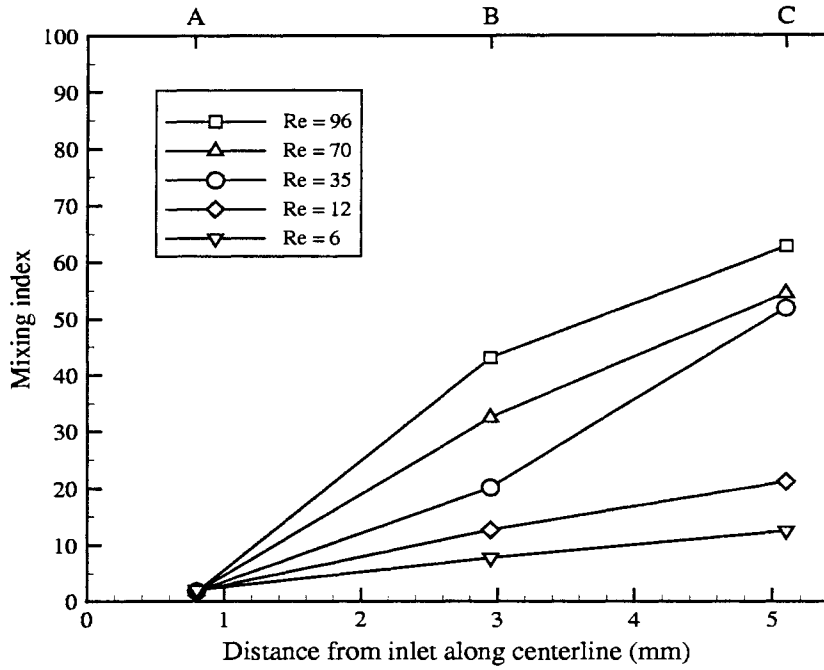


Figure 5.5 Mixing index versus centerline distance in the twisted microchannel for various Reynolds numbers.

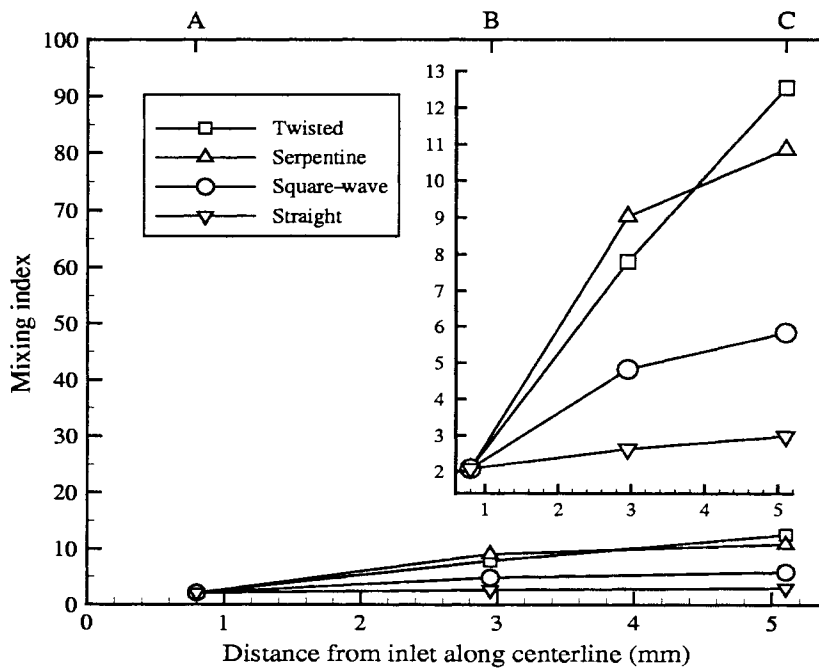


Figure 5.6 Mixing index versus centerline distance in different microchannels for the Reynolds number of 6.

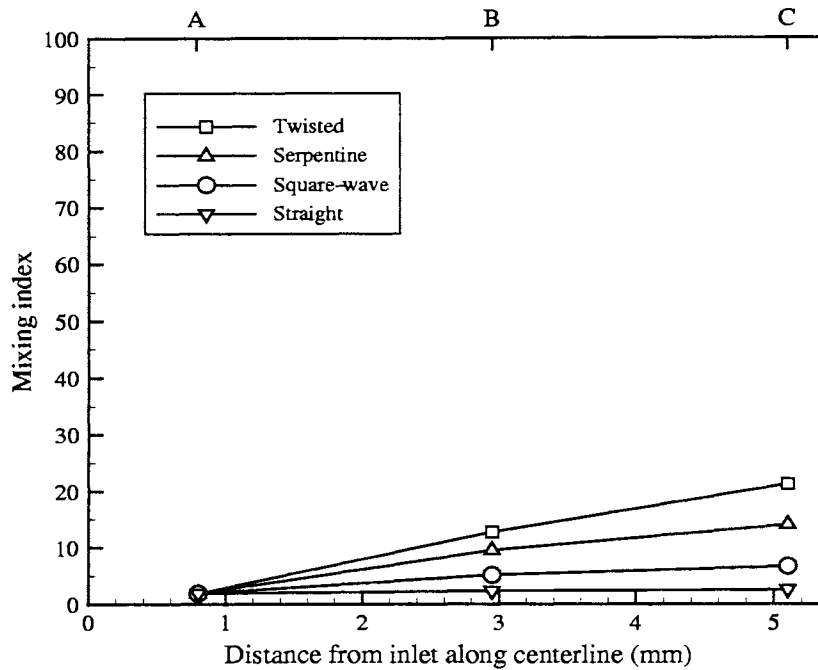


Figure 5.7 Mixing index versus centerline distance in different microchannels for the Reynolds number of 12.

of 6. It is observed that the square-wave microchannel has performed almost twice as well as the straight microchannel. However, its performance is not as well as the serpentine and twisted microchannels. Interestingly, the mixing index in the serpentine microchannel is slightly higher than the twisted microchannel at section *B*. However, the mixing index for the twisted microchannel at section *C* is the highest (12.5).

The Reynolds number of 12 is shown in Fig. 5.7 for the mixing index in each microchannel. It can be seen that the twisted microchannel performed the best whereas the straight microchannel has demonstrated poor mixing. The mixing index of the serpentine microchannel is second best, followed by the square-wave microchannel. No crossing in the mixing index is observed at the Reynolds number of 12 as was found for the Reynolds number 6 (Fig. 5.6).

Figure 5.8 illustrates the performance of microchannels at the Reynolds number of 35. Analogous to the case of Reynolds number 12, the twisted and straight microchan-

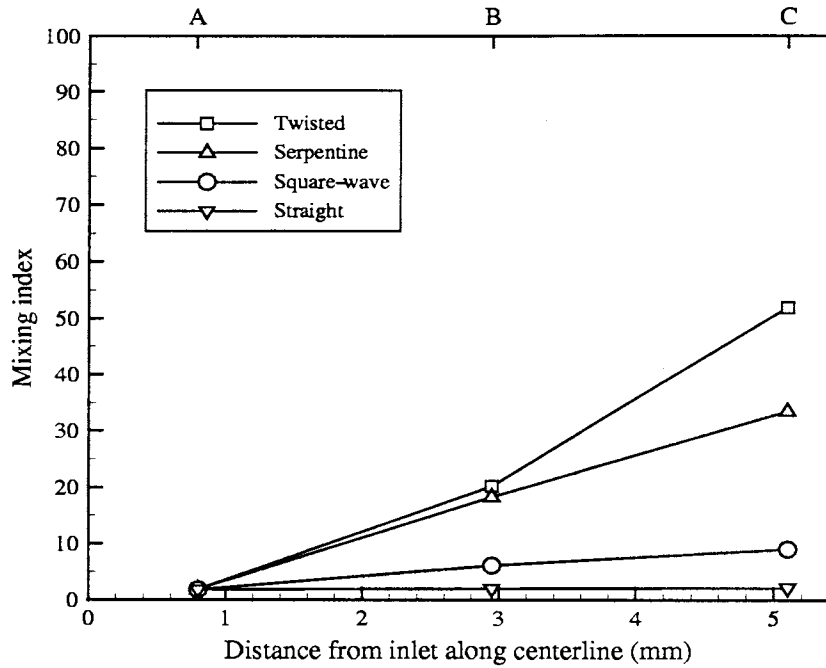


Figure 5.8 Mixing index versus centerline distance in different microchannels for the Reynolds number of 35.

nels performed as the best and the worst microchannels, respectively, in terms of the mixing index. The performance of the square-wave microchannel is also better than the straight microchannel although its performance is much less than serpentine and twisted microchannels. However, the interesting feature of this case is when the serpentine and twisted microchannels are compared. It can be observed that at section *B* the mixing indexes are very close to each other (approximately 18). However, at section *C* the mixing index of the twisted microchannel increases significantly. The mixing index for the serpentine microchannel is 33 at section *C* compared to 53 for the twisted microchannel.

Shown in Fig. 5.9 are the cases in which the Reynolds number is 70. Despite the cases for Reynolds numbers of 12 and 35, the performance of the serpentine microchannel performed the best. However, the difference in the mixing indexes between the serpentine and twisted microchannels is small, indicating both microchannels perform equally well. Furthermore, the mixing indexes of both serpentine and twisted microchannels are much

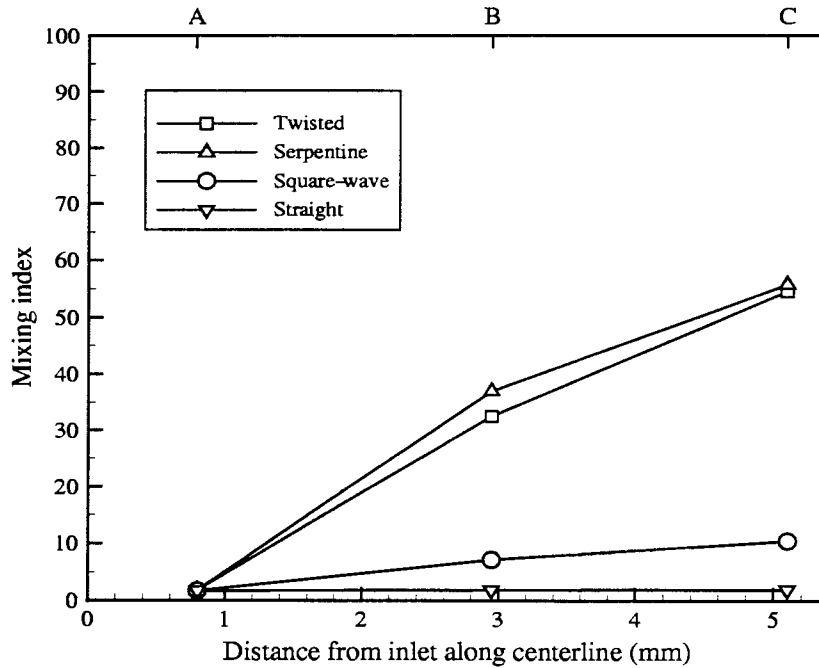


Figure 5.9 Mixing index versus centerline distance in different microchannels for the Reynolds number of 70.

higher than the square-wave microchannel and consequently the straight microchannel.

For the case of Reynolds number 96, shown in Fig. 5.10, the mixing indexes of the serpentine and twisted microchannels are almost identical. Interestingly, the mixing index in these two microchannels is significantly higher than the mixing index for the straight and square-wave microchannels.

Summarizing the data presented, the square-wave microchannel has only a marginal effect on mixing while the straight microchannel has almost no effect. On the other hand, the serpentine and twisted microchannels are better designs for the range of Reynolds numbers studied.

So far the microchannel designs were discussed quantitatively based on mixing index. Equally informative is an analysis based on density variations to demonstrate how mixing takes place in different microchannels. Therefore, to better understand and analyze the process of mixing, contour plots of density at sections *A*, *B*, and *C* are shown

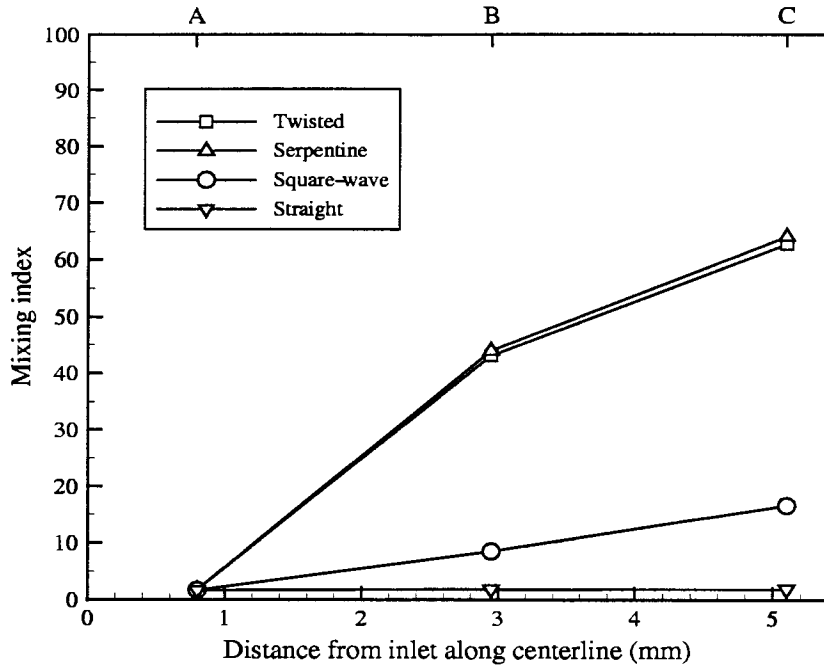


Figure 5.10 Mixing index versus centerline distance in different microchannels for the Reynolds number of 96.

in Fig. 5.11–5.15 for Reynolds numbers 6–96. In these figures, blue is the density of water ( $1000 \text{ kg/m}^3$ ), red is the density of alcohol ( $800 \text{ kg/m}^3$ ), and green is the density of a fully mixed flow ( $900 \text{ kg/m}^3$ ).

Shown in Fig. 5.11 are density contours for the Reynolds number of 6 in each microchannel. It is observed that the interface of water and alcohol in the straight and square-wave microchannels (Figs. 5.11(a) and 5.11(b)) have tilted at sections *B* and *C*. This slight rotation is due to buoyancy effects since the density of water is more than the density of alcohol. The interface between the two fluids in Fig. 5.11(a) is linear at each section, whereas in Fig. 5.11(b) the interface has a slight curve due to the bends of the square-wave microchannel. In the serpentine microchannel (Fig. 5.11(c)), the relative locations of water and alcohol remain the same in each section. However, the interface has a distinct curvature in the serpentine microchannel due to the three-dimensionality of the flow. It can be seen that the alcohol has started to surround the water. The in-

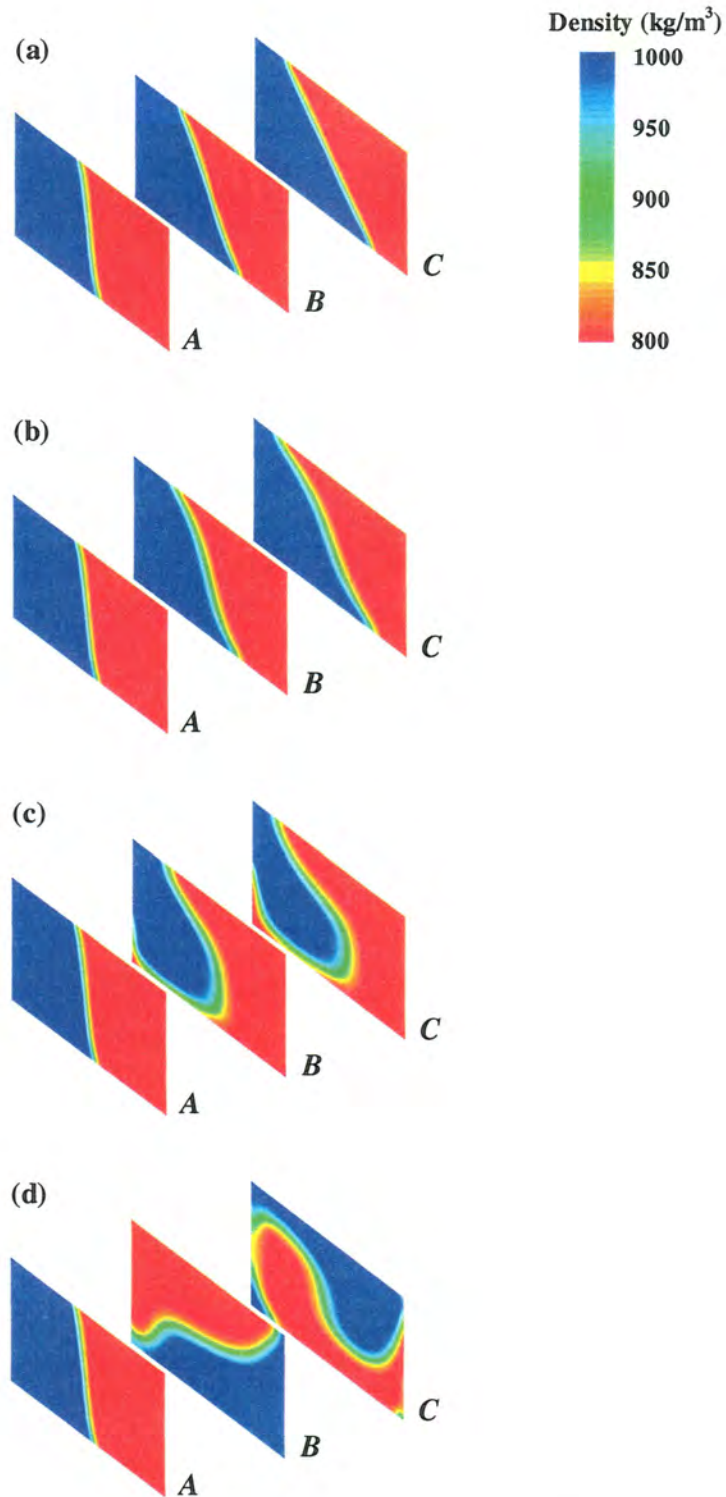


Figure 5.11 Contour plots of density at sections *A*, *B*, and *C* in (a) straight, (b) square-wave, (c) serpentine, and (d) twisted microchannels for the Reynolds number of 6.

interesting case is the twisted microchannel (Fig. 5.11(d)) in which the locations of water and alcohol have significantly changed. The water-alcohol interface rotates and twists enhancing the mixing as was shown in Fig. 5.6. Comparing Figs. 5.11(a)–5.11(d), one can observe that the onset of advection has taken place in the twisted microchannel for Reynolds number of 6.

Figure 5.12 presents the mixing trends in each microchannel for Reynolds number of 12. Again, inclinations of the interface are observed in the straight and square-wave microchannel (Figs. 5.12(a) and 5.12(b)) although the rotation is less than the corresponding cases for Reynolds number of 6. In the serpentine microchannel (Fig. 5.12(c)) the alcohol interface has almost completely enclosed the region of water. Furthermore, the water has moved towards the center of the microchannel. The trend of mixing in the twisted microchannel (Fig. 5.12(d)) is very interesting. At section *B*, alcohol surrounds the water but at section *C* water surrounds the alcohol. Thus, the twisted microchannel has displaced both fluids although a completely mixed flow has not resulted.

Illustrated in Fig. 5.13 are density contour plots for each microchannel for the Reynolds number of 35. In the straight microchannel (Fig. 5.13(a)) only a slight inclination is observed at the interface of water and alcohol at sections *B* and *C*. The water-alcohol interface for the square-wave microchannel (Fig. 5.13(b)) has become wavy with two maxima as compared to the interface for Reynolds numbers of 6 and 12. In the serpentine microchannel, shown in Fig. 5.13(c), it is observed that the interface has formed a closed circuit at section *B* with alcohol surrounding water at the center. In the twisted microchannel (Fig. 5.13(d)), it is observed that the alcohol at section *B* has been split into two regions while water is still in one region separated by alcohol. At section *C* of Fig. 5.13(d), alcohol is almost completely mixed with water such that no red regions are present. However, there are still two regions of water at the center and right side of section *C*. Comparing the serpentine and twisted microchannels, Figs. 5.13(c) and 5.13(d), green regions are visible which correspond to a mixed flow. Furthermore,

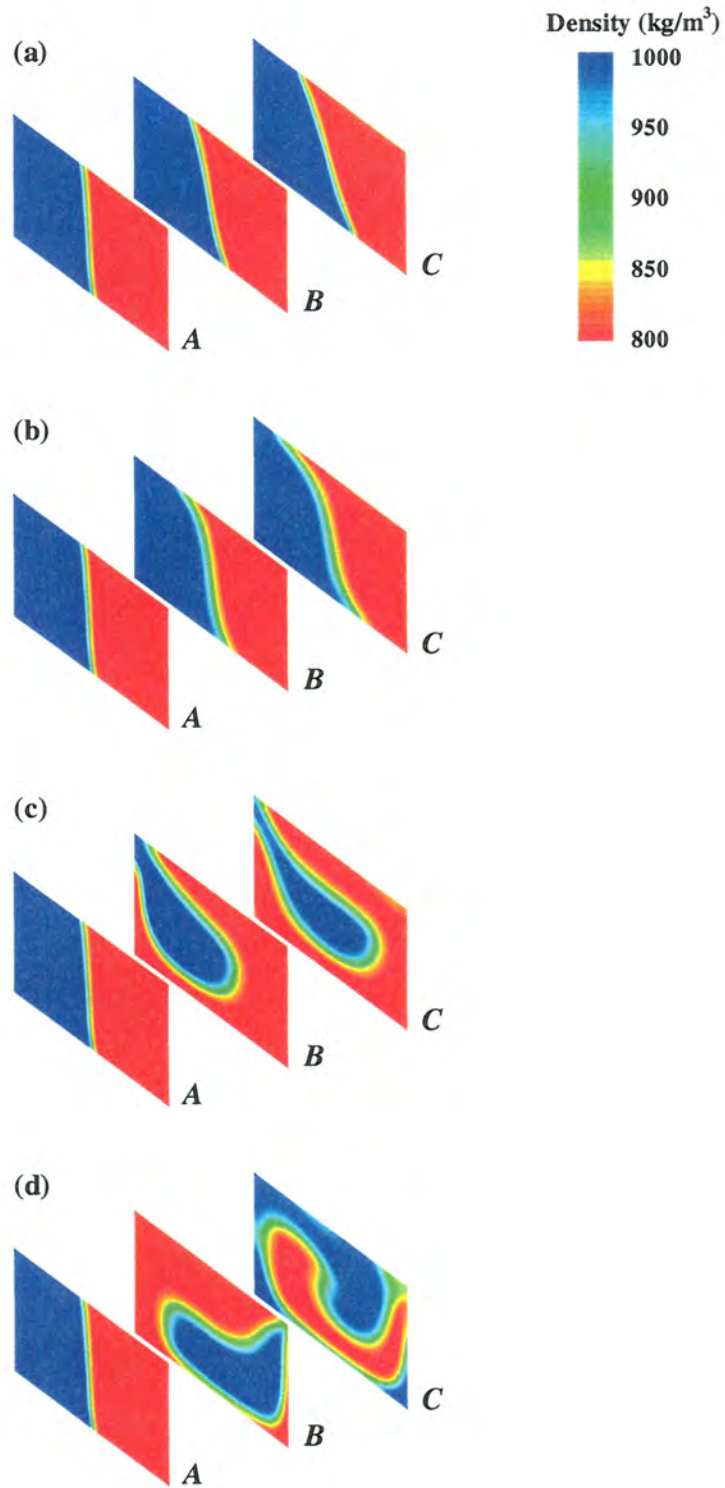


Figure 5.12 Contour plots of density at sections *A*, *B*, and *C* in (a) straight, (b) square-wave, (c) serpentine, and (d) twisted microchannels for the Reynolds number of 12.

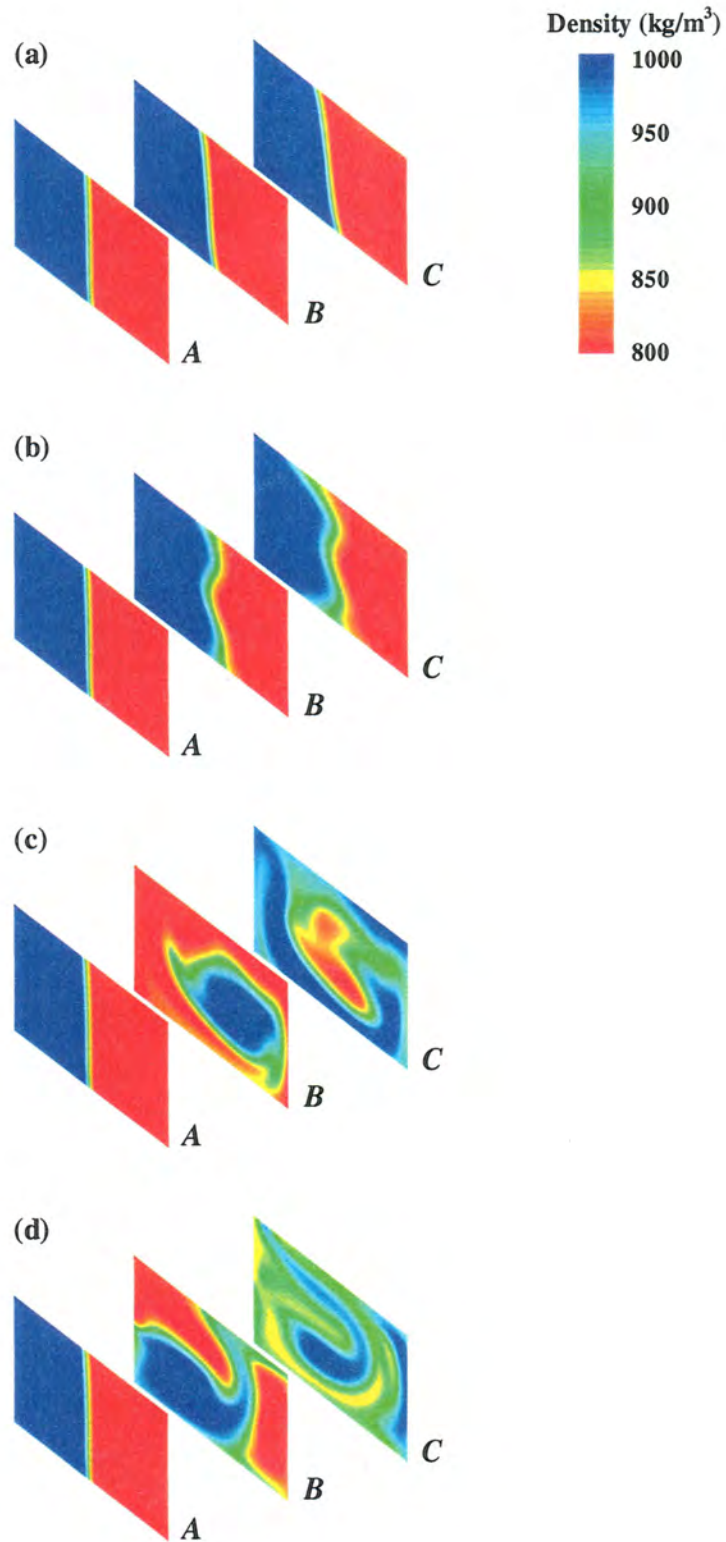


Figure 5.13 Contour plots of density at sections *A*, *B*, and *C* in (a) straight, (b) square-wave, (c) serpentine, and (d) twisted microchannels for the Reynolds number of 35.

the highest mixing index occurs in the twisted microchannel, as was shown in Fig. 5.8.

Figure 5.14 demonstrates density variation for the Reynolds number of 70 for each microchannel. A very small inclination is seen at the common boundary of water and alcohol in the straight microchannel (Fig. 5.14(a)) at section *C*. In the square-wave microchannel (Fig. 5.14(b)), maxima have become quite visible compared with the case of Reynolds number 35. In the serpentine microchannel, shown in Fig. 5.14(c), alcohol is almost completely mixed with water, while small regions of water are still observed. In the twisted microchannel, shown in Fig. 5.14(d), it is seen that at section *B* water has moved towards the bottom wall. Interestingly, at section *C*, water is still observed at the bottom even though a fully mixed region is observed on top of water.

Finally, the cases in which Reynolds number is 96 have been depicted in Fig. 5.15. Almost no inclination is seen in the straight microchannel (Fig. 5.15(a)) which substantiates that mixing is insignificant with increasing Reynolds number (refer to Fig. 5.2). The maxima of the interface of water and alcohol in the square-wave microchannel still exists while water and alcohol are penetrating into each other. Similar patterns are observed in the serpentine and twisted microchannels for the Reynolds number of 96 (Figs. 5.15(c) and 5.15(d)) as that for the Reynolds number of 70 (Figs. 5.14(c) and 5.14(d)). However, more mixed regions (green) exist for the cases of the Reynolds number of 96.

In conclusion, it was observed that advection has “seemingly” played a significant role in the serpentine and twisted microchannels while it has not taken place in the straight and square-wave microchannels effectively. In fact, it seems that “effective advection” in the serpentine and twisted microchannels has induced break up, stretching, and folding of water and alcohol therefore enhancing mixing. Furthermore, increasing the Reynolds numbers contributes to more complete mixing for the serpentine and twisted microchannels.

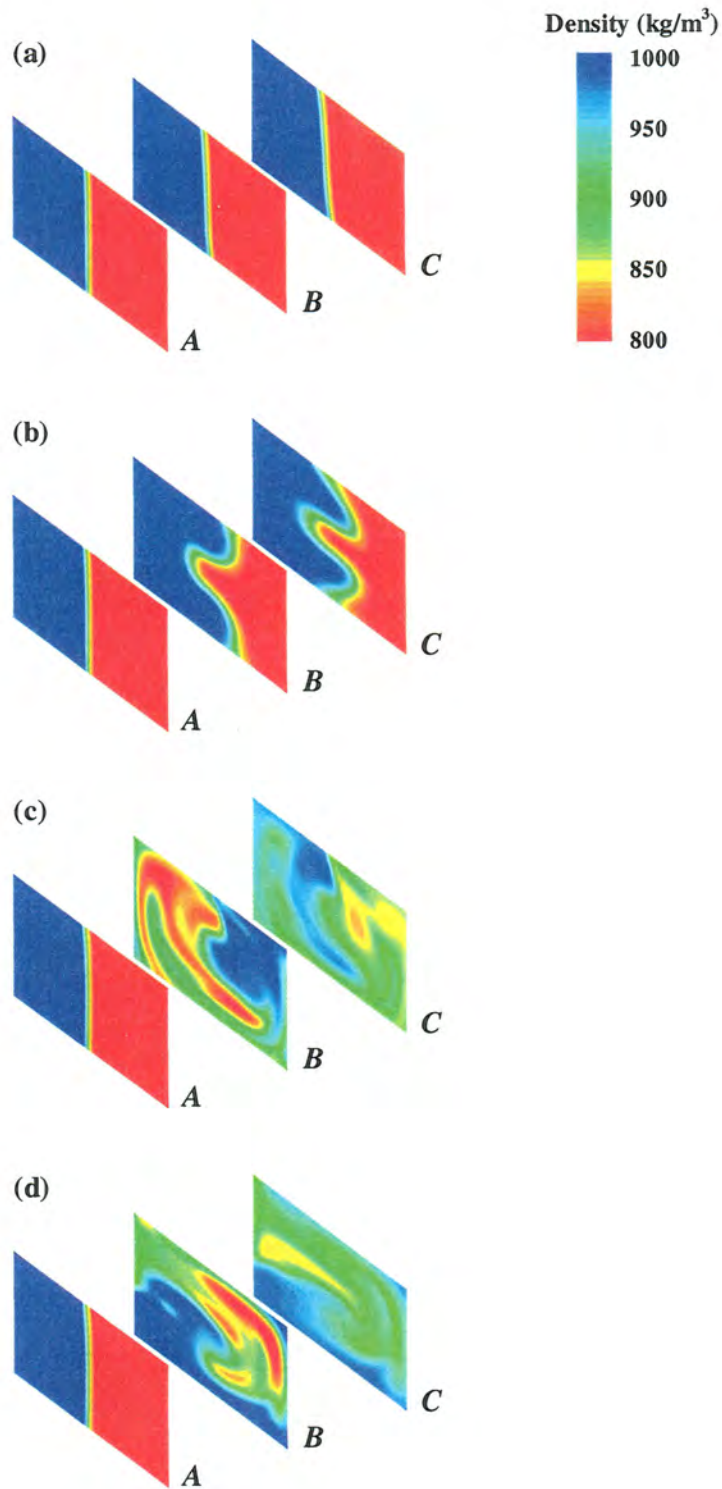


Figure 5.14 Contour plots of density at sections *A*, *B*, and *C* in (a) straight, (b) square-wave, (c) serpentine, and (d) twisted microchannels for the Reynolds number of 70.

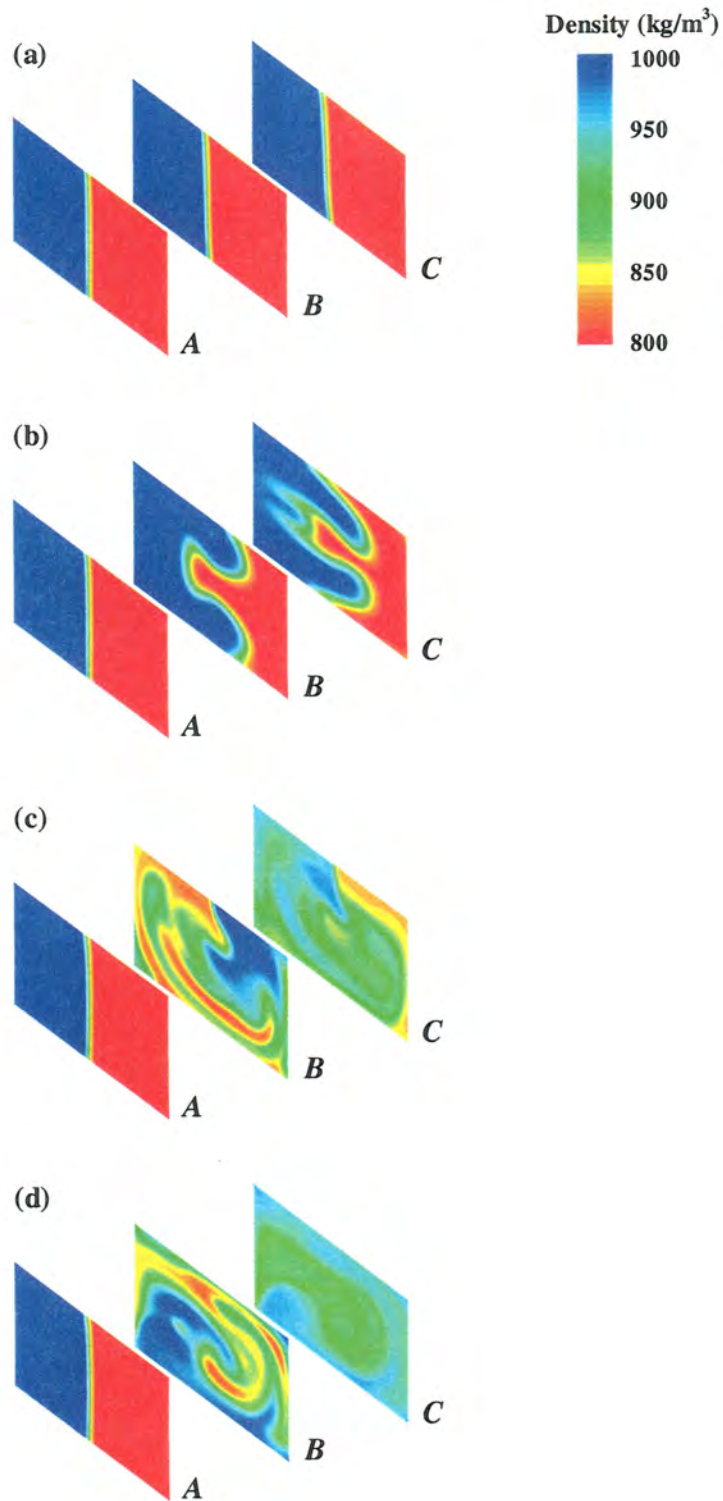


Figure 5.15 Contour plots of density at sections *A*, *B*, and *C* in (a) straight, (b) square-wave, (c) serpentine, and (d) twisted microchannels for the Reynolds number of 96.

## 5.2 Pressure Distribution

One of the important parameters in the operation of microchannels is pressure drop along the microchannel. As an example, pressure drop data are used to characterize and identify mass flow rate in microchannels. Ideally, a properly designed micromixer improves mixing performance without increasing the pressure drop. However, bends and twists result in additional pressure losses, in general. As discussed and demonstrated in Section 5.1, mixing does not enhance in the absence of bends. Therefore, it is important to measure and analyze the effects of pressure drop in microchannels with several bends.

Table 5.1 summarizes the total pressure drop (static plus dynamic pressure) in Pascal in each microchannel for the Reynolds numbers ranging between 6 and 96. The pressure loss was measured as the difference between average values of pressure on sections *A* and *C*. It can be extracted from Table 5.1 that for any microchannel, increasing the Reynolds number, increases pressure drop. However, the trend of pressure drop, while keeping the Reynolds number constant, is not similar in all microchannels. This trend can be divided into two categories based on the Reynolds number.

The Reynolds number range between 6 and 35 indicates that the straight microchannel has the largest pressure drop. On the other hand, the minimum pressure drop occurs in the twisted microchannel for the Reynolds numbers of 6 and 12, while at the Reynolds

Table 5.1 Total pressure drop (Pascal) in various microchannels between sections *A* and *C* for the Reynolds numbers ranging between 6 and 96.

Re	Microchannel			
	Straight	Square-wave	Serpentine	Twisted
<b>6</b>	110	89	73	72
<b>12</b>	220	181	154	149
<b>35</b>	641	582	533	540
<b>70</b>	1283	1397	1411	1480
<b>96</b>	1763	2212	2323	2497

number of 35, the minimum pressure drop is for the serpentine microchannel. However, the difference in the pressure drops of serpentine and twisted microchannels is very small. It is fascinating to note that despite the number of bends in the square-wave, serpentine, and twisted microchannels, pressure loss in these microchannels is less than the pressure loss in the straight microchannel.

For the Reynolds numbers of 70 and 96, the trend of pressure drop is opposite of the cases of Reynolds numbers 6–35; the minimum pressure drop occurs in the straight microchannel while the maximum pressure drop results in the twisted microchannel.

The percent difference between the lowest and highest pressure drops for constant Reynolds numbers is another interesting point of Table 5.1. These percent differences are 52.7, 47.7, 20.3, 15.4, and 41.6 for the Reynolds numbers of 6, 12, 35, 70, and 96, respectively. It is perceived that the percent difference between the maximum and minimum pressure drops decreases from Reynolds number 6 to 70. However, at Reynolds number of 96, this trend does not continue and the percent difference has increased to 41.6 unexpectedly. It is worth mentioning that by considering all microchannels and the whole range of Reynolds numbers, the smallest and the largest pressure drops have occurred for the twisted microchannel with 72 and 2497 Pa, at the Reynolds numbers of 6 and 96, respectively.

### **5.3 Evolution of Path Lines and Onset of Chaos**

In Section 5.1 mixing was studied in an Eulerian framework. It was shown that mixing enhances in serpentine and twisted microchannels more than straight and square-wave microchannels. A simple but crucial question arises in the presence of these findings, “Why?”.

To have a deeper understanding of mixing processes, it is recommended [48,107,108] to view the evolution of mixing in a Lagrangian framework. Even though a Lagrangian

viewpoint of fluid mixing is a conceptual way to study mixing processes, this viewpoint is of considerable practical importance particularly at low Reynolds numbers. In fact, the Lagrangian representation of mixing is a matter of academic curiosity since the introduction of the concept of “chaotic advection” in fluid mechanics by Aref in 1984 [6] (for an inclusive review about chaotic advection look at reference [109]).

By definition, chaotic motion means exponential separation of close trajectories [110]. Therefore, in the presence of Lagrangian chaos it is expected that the relative separation between advected tracers typically grows exponentially in space and/or time. In terms of fluid dynamics, it is perceived that small deviations in the velocity field produce large effects on chaotically advected patterns. This phenomena, which is highly complex, *can* happen even in laminar flows with very low Reynolds numbers. So, chaotic dynamics can be (and is) facilitated to achieve rapid and good mixing in low Reynolds number regimes [48, 69].

To explore the occurrence of chaotic advection in the present work, a set of massless particles were seeded in the flow along the vertical centerline of the microchannel inlet. The particles are colored so that one can recognize the locations of them in the whole domain. By tracking these particles in space and time, path lines were recorded and displayed. However, since the flow field is steady, path lines are streamlines, so integration only in space was sufficient to track each particle. The Reynolds numbers of 6 and 35 were selected to explore the idea of chaotically advected particles.

Shown in Figs. 5.16–5.19 are the traces of particles at the Reynolds number of 6 for each microchannel. It is observed that in the straight and square-wave microchannels (Figs. 5.16 and 5.17) particles have remained linear relative to each other. As was observed in Figs. 5.11(a) and (b), the interface shifts slightly toward water, the denser fluid. Furthermore, it is observed that top- and bottom-most particles have slightly separated from the other particles at the outlet. In the serpentine microchannel, shown in Fig. 5.18, a few particles have slightly diverged from the rest (dark blue and dark

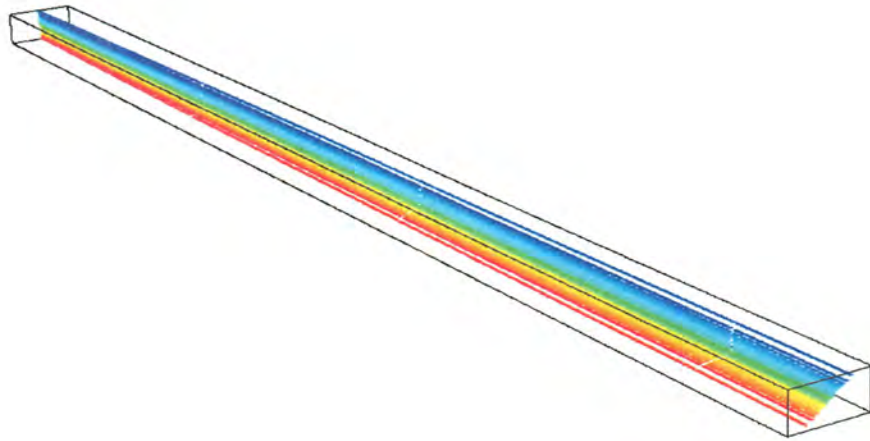


Figure 5.16 Path lines in the straight microchannel at the Reynolds number of 6. Flow is from left to right.

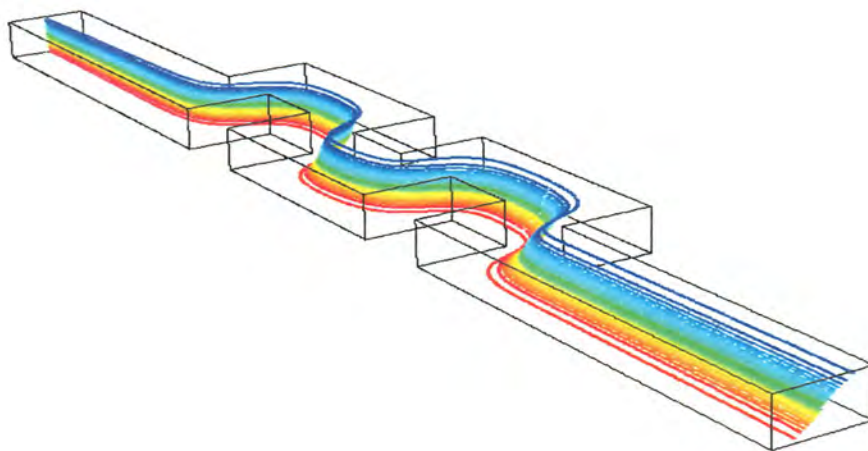


Figure 5.17 Path lines in the square-wave microchannel at the Reynolds number of 6. Flow is from left to right.

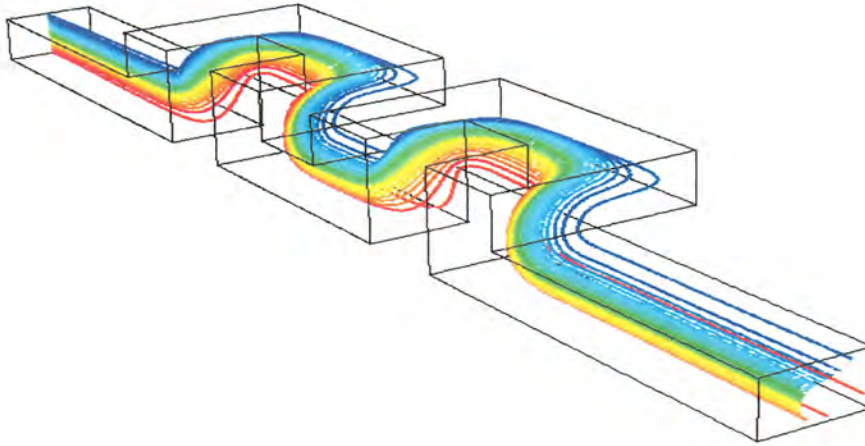


Figure 5.18 Path lines in the serpentine microchannel at the Reynolds number of 6. Flow is from left to right.

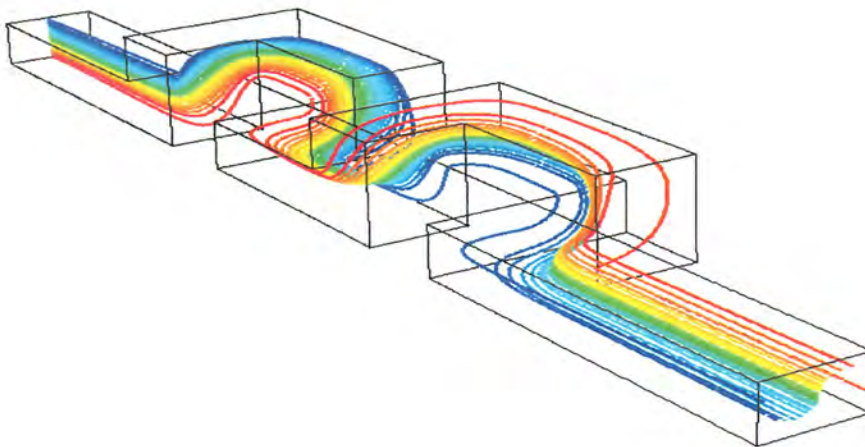


Figure 5.19 Path lines in the twisted microchannel at the Reynolds number of 6. Flow is from left to right.

red), although the initial vertical position of particles at the inlet has not changed considerably at the outlet. For the twisted microchannel, illustrated in Fig. 5.19, it is observed that after the second segment the streams of particles have twisted once. This twist has resulted in more particle displacement: from the vertical positioning at the inlet to a horizontal curvy positioning at the outlet. Comparing the serpentine and twisted microchannels (Figs. 5.18–5.19), it is revealed that in the twisted microchannel particles have wandered in the domain more than the case of the serpentine microchannel.

Figures 5.20–5.23 demonstrate the particle traces for Reynolds number of 35. By looking at the traces of particles in the straight microchannel (Fig. 5.20), there is no significant change in the relative position of particles. No separation in the position of particles has happened in the square-wave microchannel either (Fig. 5.21), even though the linear position of particles at the inlet has changed to a wavy distribution due to the sequences of bends. The note worthy cases of the Reynolds number of 35 are the serpentine and twisted microchannels illustrated in Figs. 5.22 and 5.23. It is observed that in both cases, the trajectories of particles are intertwined so that by the outlet, individual particles leaving these microchannels are significantly displaced relative to their orientation at the inlet. The completely distorted trajectories of particles in the serpentine and twisted microchannels indicate the onset of chaos in these two systems.

Based on the discussion of the serpentine and twisted microchannels for the Reynolds number of 35, once the flow passes through consecutive bends, small perturbations introduced to the flow cause trajectories to diverge exponentially from the unperturbed state. This is typical of chaotic behavior where initially small perturbations are amplified exponentially with time and/or space. As a result, diverged trajectories of particles help in the enhancement of mixing in the chaotic regime by stretching and distorting fluid elements.

It is worth noting that with the particle traces, only a small set of particles, placed at specific locations, were employed to visualize the corresponding traces. However,

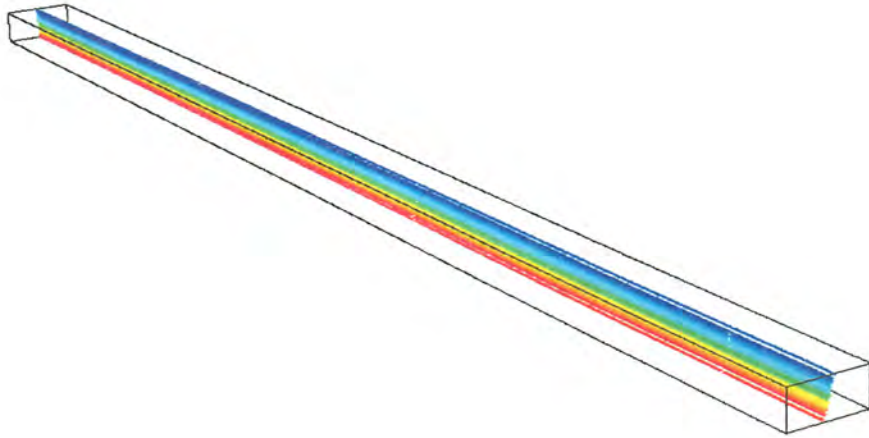


Figure 5.20 Path lines in the straight microchannel at the Reynolds number of 35. Flow is from left to right.

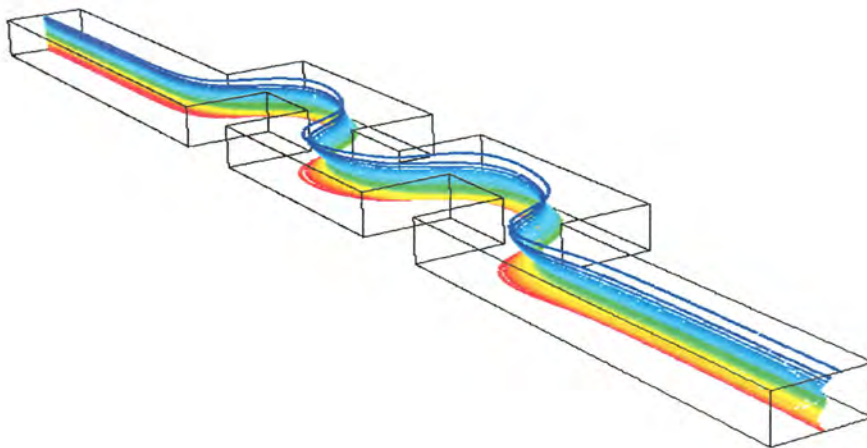


Figure 5.21 Path lines in the square-wave microchannel at the Reynolds number of 35. Flow is from left to right.

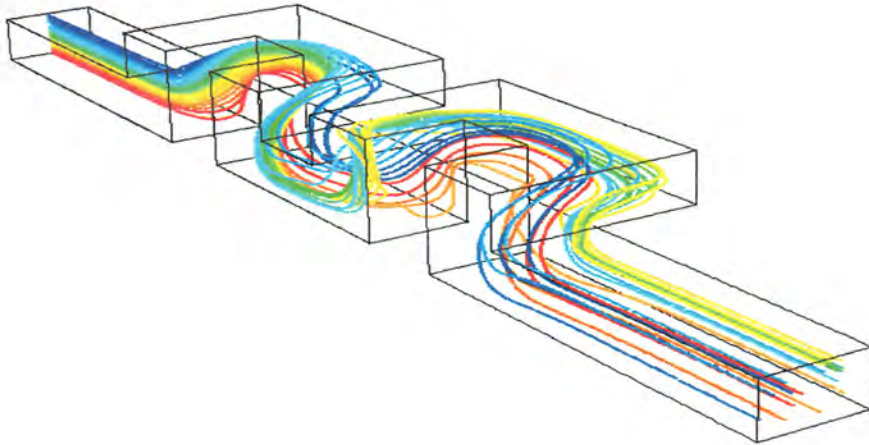


Figure 5.22 Path lines in the serpentine microchannel at the Reynolds number of 35. Flow is from left to right.

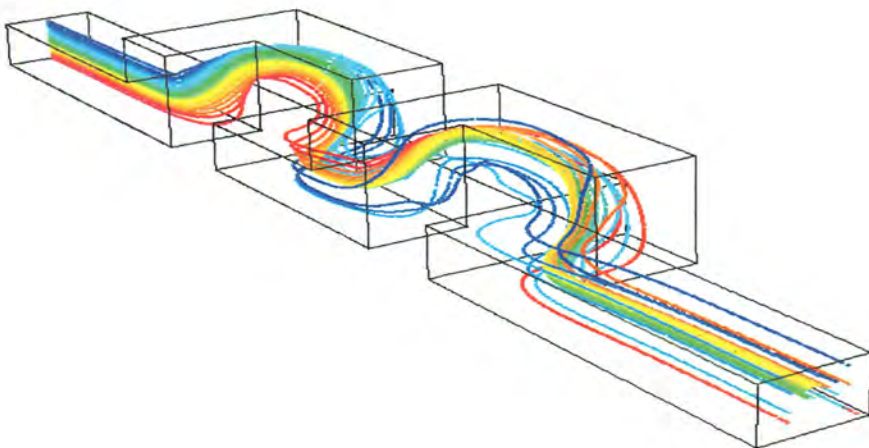


Figure 5.23 Path lines in the twisted microchannel at the Reynolds number of 35. Flow is from left to right.

examining only the advection of this small set of particles, chaotic flows existing in the serpentine and twisted microchannels were revealed. The chaotic advection could provide interactions between velocity and density fields so that small deviations in the velocity field were magnified and resulted in good mixing.

## 5.4 Correlation Between Quantitative and Qualitative Discussion of Mixing

When overall mixing index is shown versus Reynolds number, as shown in Figs. 5.24 and 5.25, the quantitative analysis of mixing index and its connection with the qualitative analysis of chaotic mixing (Section 5.3) is better understood.

Figure 5.24 depicts the mixing index at section *B*, which is after the first segment of each microchannel. It is observed that in the whole range of the Reynolds numbers studied, the serpentine and twisted microchannels have performed better than straight and square-wave microchannels, particularly at larger Reynolds numbers such as 70 and 96. However, there is a negligible difference between the mixing index of the serpentine and twisted microchannels at this location for varying Reynolds numbers. Note that the mixing index of the serpentine and twisted microchannels is about 18 at the Reynolds number 35.

On the other hand, Fig. 5.25 shows the other aspect of microchannel design: the effects of spatial sequences (i.e., bends) on mixing. This figure, which depicts the mixing index at section *C* (after the second segment), shows that when the Reynolds number is 6, 70, and 96, no preference between serpentine and twisted microchannels exist. For the Reynolds number of 12, mixing index in the twisted microchannel is marginally higher than the mixing index in the serpentine microchannel. However, for Reynolds number of 35, the mixing index in the twisted microchannel is 53, which is significantly higher than 33 mixing index in the serpentine microchannel.

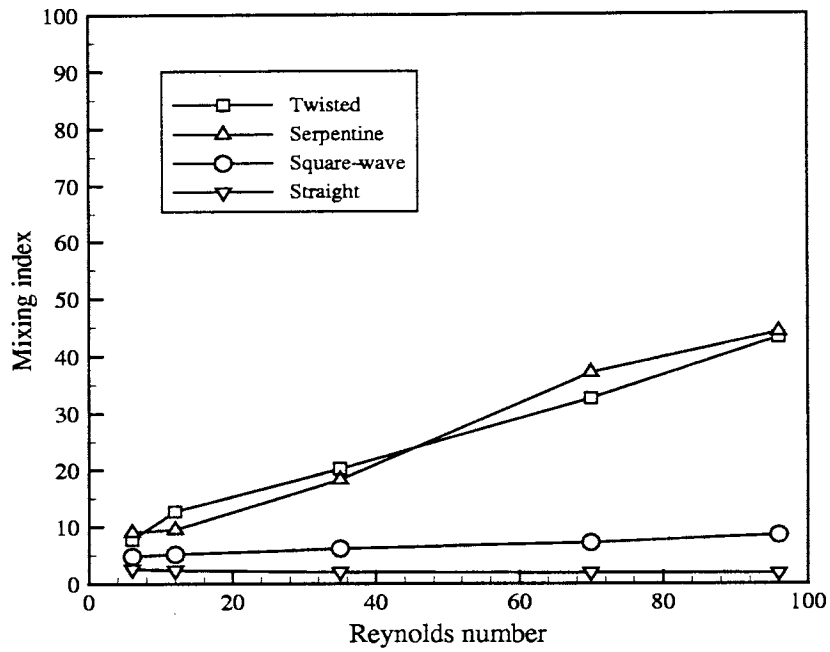


Figure 5.24 Mixing index versus Reynolds number in each microchannel at section *B*.

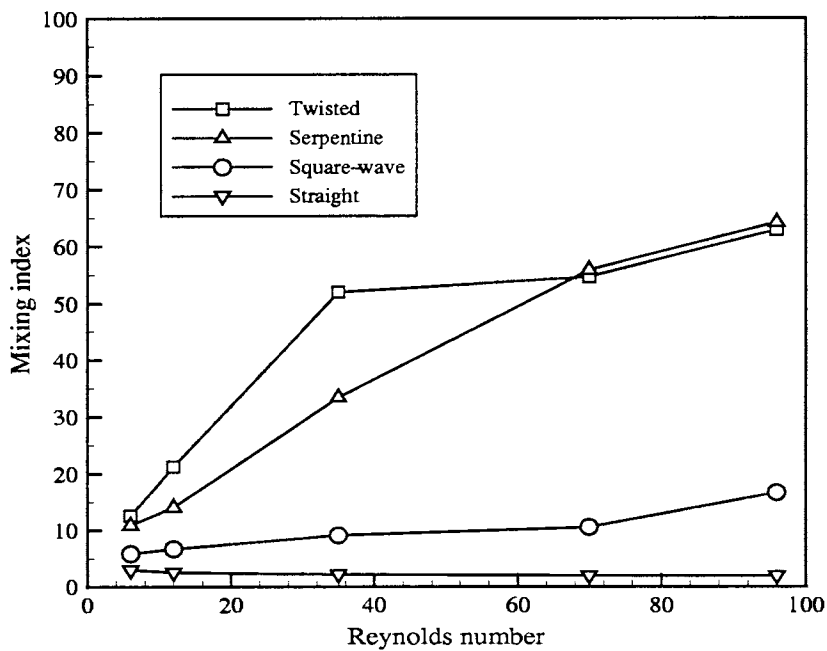


Figure 5.25 Mixing index versus Reynolds number in each microchannel at section *C*.

The substantially better performance of the twisted microchannel at the Reynolds number of 35 for section *C* shows the effective role of the second segment in the design of this microchannel, on mixing. The existence of a spatially chaotic flow with a high degree of chaos at the Reynolds of 35 in the twisted microchannel is expected. The spatially chaotic flow in the serpentine microchannel should have a lower degree of chaos.

Finn and del-Castillo-Negrete [111] investigated a model for shear flows with two independent Kelvin-Helmholtz linear instabilities. They addressed the relationship between Lagrangian and Eulerian chaos in their two-dimensional model for the first time (based on the knowledge of author of this thesis). It was shown that a relationship between Lagrangian chaos, shown by trajectories of particles, and Eulerian chaos, shown by contour plots and measured by quantitative means, exists in three-dimensional flows.

## CHAPTER 6 CONCLUDING REMARKS AND RECOMMENDATIONS

### 6.1 Conclusions

In this research, the three-dimensional mixing simulations of water and alcohol streams were carried out in four types of microdevices: straight, square-wave, serpentine, and twisted microchannels. In microchannel designs, different configurations of bends and twists were considered for the enhancement of mixing. The width and height of microchannels were on the order of  $100\ \mu\text{m}$  with a hydraulic diameter of  $200\ \mu\text{m}$ . The commercial code Fluent 6.0 was used for the simulations. The mixture model was employed to account for the interactions between water and alcohol in these microchannels for Reynolds numbers between 6 and 96.

It was shown that the streams of water and alcohol do not mix well unless the core of fluids flows in three perpendicular directions consecutively. In the straight microchannel, mixing was very poor because the core of flow was one-dimensional. The square-wave configuration in which the core of flow was two-dimensional had a marginal effect on mixing in comparison with the straight microchannel. On the other hand, in both serpentine and twisted microchannels which had the characteristics to impose three-dimensional flows, mixing was enhanced significantly. Nevertheless, the mixing indexes in the serpentine and twisted microchannels varied in different ranges of the Reynolds number.

Higher mixing indexes in the serpentine and twisted microchannels, which were

caused by wandering flows, were addressed as evident signs of chaotic flows in these two microchannels. It should be emphasized that even though well-known diagnostic methods of chaos theory, such as mapping Poincaré sections or calculating Lyapunov exponents, were not applied directly, the divergence of trajectories confirmed the presence of chaos in the serpentine and twisted microchannels. Based on the higher mixing index in the twisted microchannel at the Reynolds number of 35, when compared with the serpentine microchannel, it is concluded that the degree of chaos in the twisted microchannel is higher at this Reynolds number. For Reynolds numbers of 6, 12, 70, and 96, since the mixing index in the serpentine and twisted microchannels was close to each other, it is concluded that the degree of chaos of these two microchannels is comparable.

Finally, it was shown that a relationship between Lagrangian chaos and Eulerian chaos, shown by trajectories of particles, contour plots, and quantitative measurements, exists in three-dimensional flows. Based on the knowledge of the thesis author, this is the first time that such a relationship has been proposed and investigated.

## 6.2 Open Questions

To extend the present work, the following questions may be considered as new research for future investigations:

1. What is the best aspect ratio of the width to the height of channels in serpentine and twisted microchannels in terms of mixing?
2. What if the scale of the microchannel is reduced to the order of 10 or even 1  $\mu\text{m}$ ? Which microchannel design can enhance mixing best: serpentine or twisted microchannel? Should another configuration be proposed?
3. How does the mixing of other categories of two-phase flows take place in the suggested microchannels? For instance, gas-solid and gas-liquid flows.

4. Are the microchannel designs sufficiently effective to be applied as blood analyzers and immunoassays?
5. What are Poincaré sections of flow in the serpentine and twisted microchannels for different Reynolds numbers? What are the Lyapunov exponents of flow in these two microchannels? Which values are the degrees of chaos in the serpentine and twisted microchannels?

## BIBLIOGRAPHY

- [1] Feynman, R.P., 1992, There's Plenty of Room at the Bottom, (Transcript of a talk given by Richard P. Feynman on December 29, 1959, at the Annual Meeting of the American Physical Society, held at the California Institute of Technology), *Journal of Micromechanics and Microengineering*, **1**.
- [2] Feynman, R.P., 1993, Infinitesimal Machinery, (Manuscript from a talk given by Richard P. Feynman on February 23, 1983 at the Jet Propulsion Laboratory in the National Aeronautics and Space Administration (NASA), Pasadena, CA), *Journal of Micromechanics and Microengineering*, **2**, pp. 4-14.
- [3] Gad-el Hak, M. (Editor), 2002, *The MEMS Handbook*, CRC Press, Boca Raton, Florida.
- [4] Lorenz, E.N., 1963, Deterministic Non-periodic Flow, *Journal of Atmospheric Sciences*, **20**, pp. 130-141.
- [5] Manneville, P., 1990, *Dissipative Structures and Weak Turbulence*, Academic Press, INC., San Diego, California.
- [6] Aref, H., 1984, Stirring by Chaotic Advection, *Journal of Fluid Mechanics*, **143**, pp. 1-21.
- [7] Aref, H., 1990, Chaotic Fluid Dynamics and Turbulent Flow, *Workshop Proceedings of Whither Turbulence - Turbulence at the Crossroads*, Springer-Verlag, New York.

- [8] Bryden, M. D. and Brenner, H., 1999, Mass-transfer Enhancement via Chaotic Laminar Flow within a Droplet, *Journal of Fluid Mechanics*, **379**, pp. 319–331.
- [9] Liu, R.H., Stremmer, M.A., Sharp, K.V., Olsen, M.G., Santiago, J.G., Adrian, R.J., Aref, H., and Beebe, D.J., 2000, Passive Mixing in a Three-Dimensional Serpentine Microchannel, *Journal of Microelectromechanical Systems*, **9**, pp. 190–197.
- [10] Stremmer, M.A., Olsen, M.G., Adrian, R.J., Aref, H., Jo, B.H., and Beebe, D.J., 2000, Chaotic Mixing in Microfluidic Systems, *Solid State Sensor and Actuator Workshop*, Hilton Head, South Carolina.
- [11] Ho, C.M. and Tai, Y.C., 1998, Micro-Electro-Mechanical-Systems (MEMS) and Fluid Flows, *Annual Review of Fluid Mechanics*, **30**, pp. 579–612.
- [12] Gad-el Hak, M., 1999, The Fluid Mechanics of Microdevices – The Freeman Scholar Lecture, *Journal of Fluids Engineering*, **121**, pp. 5–33.
- [13] Knudsen, M., 1909, Die gesetze der molekularströmung und der inneren riebungsströmung der gase durch röhren, *Annalen der Physik*, **28**, pp. 75–130.
- [14] Knudsen, M., 1910, Eine revision der gleichgewichtsbedingung der gas thermische molekularströmung, *Annual Physics*, **31**, pp. 205–229.
- [15] Knudsen, M., 1910, Thermischer molekulardruck der gas in röhren, *Annual Physics*, **33**, pp. 1435–1448.
- [16] Mo, G. and Rosenberger, F., 1990, Molecular-Dynamics Simulation of Flow in a Two-Dimensional Channel with Atomically Rough Walls, *Physics Review A*, **42**, pp. 4688–4692.
- [17] Allen, M.P. and Tildesley, D.J., 1994, *Computer Simulation of Liquids*, Clarendon Press, Oxford.

- [18] Koplik, J., Banavar, J., and Willemsen, 1989, Molecular Dynamics of Fluid Flow at Solid Surfaces, *Physics of Fluids A*, **1**, pp. 781–794.
- [19] Koplik, J. and Banavar, J., 1995, Continuum Deductions from Molecular Hydrodynamics, *Annual Review of Fluid Mechanics*, **27**, pp. 257–292.
- [20] Lee, S.Y.K., Wang, M., and Zohar, Y., 2001, Gas Flow in Microchannels with Bends, *Journal of Micromechanics and Microengineering*, **11**, pp. 635–644.
- [21] Jie, D., Diago, X., Cheong, K.B., and Yong, L.K., 2000, Navier-Stokes Simulations of Gas Flow in Micro Devices, *Journal of Micromechanics and Microengineering*, **10**, pp. 372–379.
- [22] Beskok, A., 1999, A Model for Flows in Channels, Pipes, and Ducts at Micro and Nano Scales, *Microscale Thermophysical Engineering*, **3**, pp. 43–77.
- [23] Pong, K.C., Ho, C.M., Liu, J., and Tai, Y.C., 1994, Non-Linear Pressure Distribution in Uniform Microchannels, *Proceedings of the 1994 International Mechanical Engineering Congress and Exposition*, ASME, Chicago, Illinois.
- [24] Beskok, A. and Karniadakis, G.E., 1994, Simulation of Heat and Momentum Transfer in Complex Microgeometries, *Journal of Thermophysics and Heat Transfer*, **8**, pp. 647–655.
- [25] Beskok, A. and Karniadakis, G.E., 1999, A Model for Flows in Channels, Pipes, and Ducts at Micro and Nano Scales, *Microscale Thermophysical Engineering*, **3**, pp. 43–77.
- [26] Karniadakis, G.E. and Beskok, A., 2002, *Micro Flows*, Springer-Verlag, New York.
- [27] Karniadakis, G.E. and Sherwin, S., 1999, *Spectral/hp Element Methods for CFD*, Oxford University Press, New York.

- [28] Lee, W.Y., Lee, S.Y.K., Wang, M., and Zohar, Y., 2000, Microchannels in Series with Gradual Contraction/Expansion, *Proceedings of International Mechanical Engineering Congress and Exposition*, ASME MEMS, Orlando, Florida, pp. 467–472.
- [29] Arkilic, E.B., Schmidt, M.A., and Breuer, K.S., 1997, Gaseous Slip Flow in Long Microchannels, *Journal of Microelectromechanical Systems*, **6**, pp. 167–178.
- [30] Stone, H.A. and Kim, S., 2001, Microfluidics: Basic Issues, Applications, and Challenges, *AIChE Journal*, **47**, pp. 1250–1254.
- [31] Poiseuille, J., 1846, Experimental Investigations upon the Flow of Liquids in Tubes of Very Small Diameters, *Sciences Mathematiques et Physiques*, **9**, pp. 433–545.
- [32] Santiago, J.G., Wereley, S.T., Meinhart, C.D., Beebe, D.J., and Adrian, R.J., 1998, A Particle Image Velocimetry System for Microfluidics, *Experiments in Fluids*, **25**, pp. 316–319.
- [33] Kamholz, A.E., Weigl, B.H., Finlayson, B.A., and Yager, P., 1999, Quantitative Analysis of Molecular Interaction in a Microfluidic Channel: The T-Sensor, *Analytical Chemistry*, **71**, pp. 5340–5347.
- [34] Whitesides, G.M. and Strook, A.D., 2001, Flexible Methods for Microfluidics, *Physics Today*, **54**, pp. 42–48.
- [35] Meinhart, C.D., Wereley, S.T., and Santiago, J.G., 2000, A PIV Algorithm for Estimating Time-Averaged Velocity Fields, *Journal of Fluids Engineering*, **122**, pp. 285–289.
- [36] Tretheway, D.C. and Meinhart, C.D., 2002, Apparent Fluid Slip at Hydrophobic Microchannel Walls, *Physics of Fluids*, **14**, pp. L9–L12.

- [37] Wang, B.W. and Peng, X., 1994, Experimental Investigation on Forced Flow Convection of Liquid Flow through Microchannels, *International Journal of Heat and Mass Transfer*, **37**, pp. 73–82.
- [38] Peng, X.F., Petersn, G.P., and Wang, B.X., 1994, Frictional Flow Characteristics of Water Flowing Rectangular Microchannels, *Experimental Heat Transfer*, **7**, pp. 249–264.
- [39] Xu, D., Ng, T.Y., Pan, L.S., Lam, K.Y., and Li, H., 2001, Numerical Simulations of Fully Developed Turbulent Liquid Flows in Micro Tubes, *Journal of Micromechanics and Microengineering*, **11**, pp. 175–180.
- [40] Mala, Gh.M. and Li, D., 1999, Flow Characteristics of Water in Microtubes, *International Journal of Heat and Fluid Flow*, **20**, pp. 142–148.
- [41] Gravesen, P., Branebjerg, J., and Jensen, O.S., 1993, Microfluidics – A Review, *Journal of Micromechanics and Microengineering*, **3**, pp. 168–182.
- [42] Triplett, K.A., Ghiaasiaan, S.M., Abdel-Khalik, S.I., LeMouel, A., and McCord, B.N., 1999, Gas-Liquid Two-Phase Flow in Microchannels, Part II: Void Fraction and Pressure Drop, *International Journal of Multiphase Flow*, **25**, pp. 395–410.
- [43] Triplett, K.A., Ghiaasiaan, S.M., Abdel-Khalik, S.I., and Sadowski, D.L., 1999, Gas-Liquid Two-Phase Flow in Microchannels, Part I: Two-Phase Flow Patterns, *International Journal of Multiphase Flow*, **25**, pp. 377–394.
- [44] Thompson, P. and Troian, S., 1997, A General Boundary Condition for Liquid Flow at Solid Surfaces, *Nature*, **389**, pp. 359–362.
- [45] Nie, X., Doolen, G.D., and Chen, S., 2002, Lattice-Boltzman Simulations of Fluid Flows in MEMS, *Journal of Statistical Physics*, **107**, pp. 279–289.

- [46] Yang, C., Li, D.Q., and Masliyah, J.H., 1998, Modeling Forced Liquid Convection in Rectangular Microchannels with Electrokinetic Effects, *International Journal of Heat and Mass Transfer*, **41**, pp. 4229–4249.
- [47] Qu, W.L., Mala, G.M., and D.Q., Li, 1999, Pressure Driven Water Flows in Trapezoidal Silicon Microchannels, *International Journal of Heat and Mass Transfer*, **43**, pp. 353–364.
- [48] Ottino, J.M., 1989, *The Kinematics of Mixing: Stretching, Chaos, and Transport*, Cambridge University Press, Cambridge.
- [49] Schwesinger, N., Frank, T., and Wurmus, H., 1996, A Modular Microfluidic System with an Integrated Micromixer, *Journal of Micromechanics and Microengineering*, **6**, pp. 99–102.
- [50] Branebjerg, J., Gravesen, P., Krog, J., and Nielsen, C., 1996, Fast Mixing by Lamination, *Proceedings of the IEEE Micro Electro Mechanical Systems (MEMS)*, IEEE, San Diego, California, pp. 441–446.
- [51] Bertsch, A., Heimgartner, S., Cousseau, P., and Renaud, P., 2001, 3D Micromixers – Downscaling Large Scale Industrial Static Mixers, *Proceedings of the 14th IEEE International Micro Electro Mechanical Systems Conference (MEMS'01)*, IEEE, Interlaken, Switzerland, pp. 507–510.
- [52] Yi, M. and Bau, H.H., 2000, The Kinematics of Bend-Induced Stirring in Micro-Conduits, *Proceedings of the 2000 ASME International Mechanical Engineering Congress and Exposition, MEMS*, Baltimore, Maryland, pp. 489–496.
- [53] Gobby, D., Angeli, P., and Gavriilidis, A., 2001, Mixing Characteristics of T-Type Microfluidic Mixers, *Journal of Micromechanics and Microengineering*, **11**, pp. 126–132.

- [54] Johnson, T.J., Ross, D., and Locascio, 2002, Rapid Microfluidic Mixing, *Analytical Chemistry*, **74**, pp. 45–51.
- [55] Wang, H., Iovenitti, P., Harvey, E., and S., Masood, 2002, Optimizing Layout of Obstacles for Enhanced Mixing in Microchannels, *Smart Materials and Structures*, **11**, pp. 662–667.
- [56] Kaye, B.H., 1993, *Chaos & Complexity: Discovering the Surprising Patterns of Science and Technology*, John Wiley & Sons Ltd., New York.
- [57] Hilborn, C.H., 1994, *Chaos and Nonlinear Dynamics*, Oxford University Press, New York.
- [58] Cambel, A.B., 1993, *Applied Chaos Theory: A Paradigm for Complexity*, Academic Press, INC., California.
- [59] Lesne, A., 1998, *Renormalization Methods : Critical Phenomena, Chaos, Fractal Structures*, John Wiley & Sons Ltd., New York.
- [60] Moon, F.C., 1992, *Chaotic and Fractal Dynamics*, John Wiley & Sons Inc., New York, 2nd edition.
- [61] Glendinning, P., 1994, *Stability, Instability and Chaos: An Introduction to the Theory of Nonlinear Differential Equations*, Cambridge University Press, New York.
- [62] Wiggins, S., 1990, *Introduction to Applied Nonlinear Dynamical Systems and Chaos*, Springer-Verlag, New York.
- [63] Wiggins, S., 1992, *Chaotic Transport in Dynamical Systems*, Springer-Verlag, New York.

- [64] H.-L., Dai and R.W., Field, 1995, *Molecular Dynamics and Spectroscopy by Stimulated Emission Pumping*, Advanced Series in Physical Chemistry, Vol. 4, World Scientific Publishing Co., New Jersey.
- [65] Peterson, I., 1993, *Newton's Clock: Chaos in the Solar System*, W.H. Freeman & Co., New York.
- [66] Dankowicz, H., 1998, *Chaotic Dynamics in Hamiltonian Systems: With Applications to Celestial Mechanics*, World Scientific Series on Nonlinear Science, Series A, Vol. 25, World Scientific Publishing Co., New Jersey.
- [67] Benest, D. and Froeschle, C. (Editors), 2002, *Singularities in Gravitational Systems: Applications to Chaotic Transport in the Solar System*, Springer-Verlag, New York.
- [68] Kontopoulos, G.I. and Contopoulos, G., 2002, *Order and Chaos in Dynamical Astronomy*, Springer-Verlag, New York.
- [69] Aref, H. and El Naschie, M.S. (Editors), 1995, *Chaos Applied to Fluid Mixing*, Pergamon Press, London.
- [70] Aref, H. and Stremler, M.A., 1999, Four-Vortex Motion with Zero Total Circulation and Impulse, *Physics of Fluids*, **11**, pp. 3704–3715.
- [71] Stremler, M.A. and Aref, H., 1999, Motion of Three Point Vortices in a Periodic Parallelogram, *Journal of Fluid Mechanics*, **392**, pp. 101–128.
- [72] Boyland, P.L., Aref, H., and Stremler, M.A., 2000, Topological Fluid Mechanics of Stirring, *Journal of Fluid Mechanics*, **403**, pp. 277–304.
- [73] Aref, H., 2002, A Transformation of the Point Vortex Equations, *Physics of Fluids*, **14**, pp. 2395–2401.

- [74] Jones, S.W., Thomas, O.M., and Aref, H., 1989, Chaotic Advection by Laminar Flow in a Twisted Pipe, *Journal of Fluid Mechanics*, **209**, pp. 335–357.
- [75] Ottino, J.M., 1992, New Applications of Chaos in Chemical Engineering: Intuition versus Prediction, *Applied Chaos*, Kim, J.H. and Stringer, J., editors, pp. 143–174, John Wiley & Sons Ltd., New York.
- [76] Khakhar, D.V., Franjione, J.G., and Ottino, J.M., 1987, A Case Study of Chaotic Mixing in Deterministic Flows: The Partitioned Pipe Mixer, *Chemical Engineering Science*, **42**, pp. 2909–2926.
- [77] Niederkorn, T.C. and Ottino, J.M., 1993, Mixing of a Viscoelastic Fluid in a Time-Periodic Flow, *Journal of Fluid Mechanics*, **256**, pp. 243–268.
- [78] Niederkorn, T.C. and Ottino, J.M., 1994, Chaotic Mixing of Shear-Thinning Fluids, *AIChE Journal*, **40**, pp. 1782–1793.
- [79] Aref, H. and Balachandar, S., 1986, Chaotic Advection in a Stokes Flow, *Physics of Fluids*, **29**, pp. 3515–3521.
- [80] Zalc, J.M. and Muzzio, F.J., 1999, Parallel-Competitive Reactions in a Two-Dimensional Chaotic Flow, *Chemical Engineering Science*, **54**, pp. 1053–1069.
- [81] Hill, K.M., Gilchrist, J.F., Ottino, J.M., Khakhar, D.V., and McCarthy, J.J., 1999, Mixing of Granular Materials: A Test-Bed Dynamical System for Pattern Formation, *International Journal of Bifurcation and Chaos*, **9**, pp. 1467–1484.
- [82] Khakhar, D.V., McCarthy, J.J., Gilchrist, J.F., and Ottino, J.M., 1999, Chaotic Mixing of Granular Materials in Two-Dimensional Tumbling Mixers, *CHAOS*, **9**, pp. 195–205.

- [83] Bondar, F. and Battaglia, F., 2002, Bifurcation Analysis of Mixing Actuated by Time-Periodic Vortices, *Proceedings of the 2002 ASME International Mechanical Engineering Congress and Exposition*, ASME Paper FED-33288, New Orleans, Louisiana.
- [84] D'Alessandro, D., Dahleh, M., and Mezic, I., 1997, Maximum Entropy Approach to the Control of Mixing, *Proceedings of the American Control Conference*, IEEE, Albuquerque, New Mexico, pp. 160–161.
- [85] D'Alessandro, D., Dahleh, M., and Mezic, I., 1999, Control of Mixing in Fluid Flow: A Maximum Entropy Approach, *IEEE Transactions on Automatic Control*, **44**, pp. 1852–1863.
- [86] Miles, K.C., Nagarajan, B., and Zumbrennen, D. A., 1995, Three-Dimensional Chaotic Mixing of Fluids in a Cylindrical Cavity, *Journal of Fluids Engineering*, **117**, pp. 582–588.
- [87] Cartwright, J.H.E., Feingold, M., and Piro, O., 1996, Chaotic Advection in Three-dimensional Unsteady Incompressible Laminar Flow, *Journal of Fluid Mechanics*, **316**, pp. 259–284.
- [88] Rothstein, D., Henry, E., and Gollub, J.P., 1999, Persistent Patterns in Transient Chaotic Fluid Mixing, *Nature*, **401**, pp. 770–772.
- [89] Lee, Y.K., Tabeling, P., Shih, C., and Ho, C.M., 2000, Characterization of a MEMS-Fabricated Mixing Device, *Proceedings of MEMS, ASME International Mechanical Engineering Fabricated Mixing Device*, ASME MEMS, Orlando, Florida.

- [90] Lee, Y., Deval, J., Tabeling, P., and Ho, C., 2001, Chaotic Mixing in Electrokinetically and Pressure Driven Micro Flows, *Proceedings of the 14th IEEE Workshop on MEMS*, IEEE MEMS, Interlaken, Switzerland, pp. 483–486.
- [91] Jones, S.W. and Aref, H., 1988, Chaotic Advection in Pulsed Source-Sink Systems, *Physics of Fluids*, **31**, pp. 469–485.
- [92] Koch, M., Witt, H., Evans, A.G.R., and Brunnschweiler, A., 1999, Improved Characterization Technique for Micromixers, *Journal of Micromechanics and Microengineering*, **9**, pp. 156–158.
- [93] Stroock, A.D., Dertinger, S.K.W., Armand, A., Mezic, I., Stone, H.A., and G.M., Whitesides, 2002, Chaotic Mixer for Microchannels, *Science*, **295**, pp. 647–651.
- [94] Niu, X. and Lee, Y.K., 2003, Efficient Spatial-Temporal Chaotic Mixing in Microchannels, *Journal of Micromechanics and Microengineering*, **13**, pp. 454–462.
- [95] Beebe, D.J., Adrian, R.J., Olsen, M.G., Stremmer, M.A., Aref, H., and Jo, B.-H., 2001, Passive Mixing in Microchannels: Fabrication and Flow Experiments, *Mechanics & Industries*, **2**, pp. 343–348.
- [96] Fluent Incorporated, 2001, *Fluent 6.0 User's Manual*, Fluent Inc., Lebanon, New Hampshire.
- [97] Pai, S., 1977, *Two-Phase Flows*, Vieweg Tracts in Pure and Applied Physics, Vol. 3, Vieweg, Germany.
- [98] Joseph, D.D. and Renardy, Y.Y., 1993, *Fundamentals of Two-Fluid Dynamics, Part I: Mathematical Theory and Applications*, Springer-Verlag, New York.
- [99] Joseph, D.D. and Renardy, Y.Y., 1993, *Fundamentals of Two-Fluid Dynamics, Part II: Lubricated Transport, Drops and Miscible Liquids*, Springer-Verlag, New York.

- [100] Tannehill, J.C., Anderson, D.A., and Pletcher, R.H., 1997, *Computational Fluid Mechanics and Heat Transfer*, Taylor & Francis Ltd., Philadelphia, PA, 2nd edition.
- [101] Patankar, S.V., 1980, *Numerical Heat Transfer and Fluid Flow*, Hemisphere Publishing Corp., Washington, D.C.
- [102] Branebjerg, J., Fabius, F., and Gravesen, P., 1994, Application of Miniature Analyzers: From Microfluidic Components to  $\mu$ TAS, *Proceedings of the Micro Total Analysis Systems '94 Workshop*, Enschede, The Netherlands, pp. 141–151.
- [103] Aref, H., 1990, Chaotic Advection of Fluid Particles, *Philosophical Transactions of the Royal Society of London A*, **333**, pp. 273–288.
- [104] Fluent Incorporated, 2001, *Gambit 2.0 User's Manual*, Fluent Inc., Lebanon, New Hampshire.
- [105] Gerald, C.F. and Wheatley, P.O., 1999, *Applied Numerical Analysis*, Addison Wesley Longman, New York, 6th edition.
- [106] High Performance Computing Center, date retrieved: May 10th, 2003, Configuration of HPC2 machine, (<http://andrew.ait.iastate.edu/HPC2/config.html>), Durham Center, Iowa State University.
- [107] Aref, H., 1996, Application of Dynamical Systems Theory to Fluid Mechanics, *Research Trends in Fluid Dynamics*, Lumley, J.L. et al., editor, pp. 15–54, American Institute of Physics, New York.
- [108] Hinch, E.J., 1999, Mixing: Turbulence and Chaos – An Introduction, *Mixing, Chaos and Turbulence*, Chaté, H., Villermaux, E., and Chomaz, J.-M., editors, pp. 37–56, Kluwer Academic / Plenum Publishers, New York.

- [109] Aref, H., 2002, The Development of Chaotic Advection, *Physics of Fluids*, **14**, pp. 1315–1325.
- [110] Seydel, R., 1994, *Practical Bifurcation and Stability Analysis*, Springer-Verlag, New York, 2nd edition.
- [111] Finn, J.M. and del Castillo-Negrete, D., 2001, Lagrangian Chaos and Eulerian Chaos in Shear Flow Dynamics, *CHAOS*, **11**, pp. 816–832.

## BIOGRAPHICAL SKETCH

On September thirteenth, 1974, Farshid Bondar was born in Tehran, Iran. He started his studies in the Department of Mechanical Engineering at the Sharif University of Technology, Tehran, Iran in 1994. As an undergraduate student, he became interested in computational fluid dynamics and the theory and applications of chaotic dynamical systems in thermo-fluid sciences. In 1999, he received the Bachelor of Science in Mechanical Engineering with a minor in Naval Architecture upon the completion of his senior project entitled “Investigation of the Role of Chaos in Fluid Mixing Optimization” under the supervision of Dr. Mohammad Taeibi-Rahni.

To pursue his studies, he attended the graduate program of Mechanical Engineering at Iowa State University in 2001. As a graduate research assistant, his focus was on computational modeling in microfluidics and the design of chaotic micromixers, with the supervision of Dr. Francine Battaglia. In 2002, he was awarded with a Professional Advancement Grant for research from Iowa State University. He was honored with lifetime membership in Tau Beta Pi engineering honor society in 2003. In the same year, he was entitled to all the privileges granted by the American Society of Mechanical Engineers. To pursue his Ph.D. studies, he will be joining the Department of Theoretical and Applied Mechanics at the University of Illinois at Urbana-Champaign in August 2003.